Multi-level transcriptomic analysis of *LMNA*-related dilated cardiomyopathy identifies disease-driving processes

Noam Zuela-Sopilniak*[,1,2], Julien Morival*[,1,2] and Jan Lammerding[#,1,2]

[1] Weill Institute for Cell and Molecular Biology, Cornell University, Ithaca, NY, USA
[2] Meinig School of Biomedical Engineering, Cornell University, Ithaca, NY, USA
* Contributed equally
[#] Corresponding author; email: jan.lammerding@cornell.edu

Abstract. *LMNA*-related dilated cardiomyopathy (*LMNA*-DCM) is one of the most severe forms of DCM. The incomplete understanding of the molecular disease mechanisms results in lacking treatment options, leading to high mortality amongst patients. Here, using an inducible, cardiomyocyte-specific lamin A/C depletion mouse model, we conducted a comprehensive transcriptomic study, combining both bulk and single nucleus RNA sequencing, and spanning *LMNA*-DCM disease progression, to identify potential disease drivers. Our refined analysis pipeline identified 496 genes already misregulated early in disease. The expression of these genes was largely driven by disease specific cardiomyocyte sub-populations and involved biological processes mediating cellular response to DNA damage, cytosolic pattern recognition, and innate immunity. Indeed, DNA damage in *LMNA*-DCM hearts was significantly increased early in disease and correlated with reduced cardiomyocyte lamin A levels. Activation of cytosolic pattern recognition in cardiomyocytes was independent of cGAS, which is rarely expressed in cardiomyocytes, but likely occurred downstream of other pattern recognition sensors such as IFI16. Altered gene expression in cardiac fibroblasts and immune cell infiltration further contributed to tissue-wide changes in gene expression. Our transcriptomic analysis further predicted significant alterations in cell-cell communication between cardiomyocytes, fibroblasts, and immune cells, mediated through early changes in the extracellular matrix (ECM) in the *LMNA*-DCM hearts. Taken together, our work suggests a model in which nuclear damage in cardiomyocytes leads to activation of DNA damage responses, cytosolic pattern recognition pathway, and other signaling pathways that activate inflammation, immune cell recruitment, and transcriptional changes in cardiac fibroblasts, which collectively drive *LMNA*-DCM pathogenesis.

Keywords:
Cell-cell-communication, DNA damage, laminopathy, nuclear damage, transcriptomics

Introduction

Dilated cardiomyopathy (DCM) results from acquired (idiopathic or environmental) or congenital factors and is characterized by enlargement of the heart chambers, impaired systolic function, and fibrosis[1-3], culminating in cardiac dysfunction. About 6-8% of congenital DCM cases arise from mutations in the *LMNA* gene [4-8], which encodes the nuclear envelope proteins lamins A and C. Lamins are type V intermediate filaments and major constituents of the nuclear lamina, a protein meshwork underlying the inner nuclear membrane. Lamins A/C provide structural support to the nucleus and regulate numerous cellular processes, such as chromatin organization, nuclear pore positioning, signal transduction, transcriptional regulation, and DNA damage repair[9-11]. *LMNA* related dilated cardiomyopathy (*LMNA*-DCM) has worse clinical prognosis compared to other congenital forms of DCM[12-15]], predominantly due to arrhythmias, which result in high rates of sudden cardiac death, even in the absence of systolic dysfunction[13]. The molecular mechanisms of *LMNA*-related pathogenesis remain largely unresolved, presenting a major hurdle in developing effective target-oriented treatments. Current therapeutic approaches for *LMNA*-DCM have limited efficacy, resulting in ≈20% of *LMNA*-DCM patients requiring heart transplants [16].

Several signaling pathways, such as AMP-activated protein kinase (AMPK), myocardin-related transcription factor (MTRF), extracellular signal-regulated kinase 1/2 (ERK1/2), protein kinase C (AKT)/mammalian target of rapamycin (mTOR), Wnt/β-Catenin and transforming growth factor- β (TGF-β), have been found to be misregulated in *LMNA*-DCM [17, 18]. In particular, DNA damage and activation of DNA damage response pathways have been proposed as pathogenic mechanisms in striated muscle laminopathies [19-22] and suggested as predictors for patient outcome and treatment efficiency[23, 24]. Supporting this idea, cardiac tissues from individuals with *LMNA*-DCM and cardiac-specific laminopathy mouse models exhibit increased levels of DNA damage and activation of p53 [19, 20, 25]. It is unclear, however, whether these effects are disease causing or arise as downstream consequences of other defects associated with *LMNA* mutations. Furthermore, despite various attempts to target these altered signaling pathways in various *LMNA*-DCM preclinical models, none of the approaches have been curative, and most have shown only modest effects on survival [19, 22, 25-28].

To identify gene expression changes occurring early in disease-development, and thus likely constituting disease drivers, we here generated mice with tamoxifen-inducible, cardiomyocyte-specific deletion of *Lmna* (*Lmna*-cKO). The resulting depletion of lamin A/C in cardiomyocytes achieved in this model mirrors the reduced lamin A/C levels frequently found in *LMNA*-DCM patients[14, 29] and led to severe DCM and death within 3-5 weeks. Using the *Lmna*-cKO model, we performed a multi-level transcriptomic analysis of left ventricles to study the effect of lamin A/C depletion on cardiac function and disease pathogenesis. To gain further insights into the involved molecular pathways, we developed computational approaches combining the benefits of bulk RNA-seq (i.e., high sensitivity and resolution) and single-nucleus RNA-seq (i.e., cell type-specificity) to compare gene expression differences between left ventricles obtained from *Lmna*-cKO mice and littermate controls at both early and late disease stages.

We found that lamin A/C depletion resulted in DNA damage in cardiomyocytes that correlated with loss of lamin A and that preceded immune/inflammatory response. In addition, we found that a small subpopulation of cardiomyocytes was responsible for many of the tissue-level transcriptional changes, in large part mediated by cytosolic pattern recognition pathways that might respond to DNA damage and genomic DNA exposed to the cytoplasm following nuclear envelope rupture. Other cell types, particularly fibroblasts and immune cells, also contributed to the response. Furthermore, we observed a substantial change in extracellular matrix mediated cell-cell communication in hearts of *Lmna*-cKO mice. Together, our studies provide new insights into the dynamics and contribution of specific cell populations to transcriptional changes associated with *LMNA*-DCM that can guide the development of novel therapeutic strategies.

Methods

Animals. Mice expressing a transgene containing the mouse cardiac-specific α-myosin heavy chain promoter (αMHC or Myh6) directing expression of a tamoxifen-inducible Cre recombinase (MerCreMer) in juvenile and adult cardiac myocytes (αMHC-MerCreMer) and mice possessing loxP sites flanking exon 2 of the lamin A gene (*Lmna* floxed or *Lmna*$^{fl/fl}$)[[30], were obtained from The Jackson Laboratory (JAX) in a C57BL/6 background (αMHC-MerCreMer: B6.FVB(129)-A1cf$^{Tg(Myh6\text{-}cre/Esr1*)1Jmk}$/J, strain 005657; and *Lmna* floxed: *Lmna*$^{tm1.1Yxz}$/J, strain 026284, respectively) and genotyped as instructed. All mice used in this study were obtained in the same C57BL/6 genetic background and backcrossed for at least three generations. To generate the inducible, cardiac specific *Lmna* deletion mouse model (*Lmna*-cKO), αMHC-MerCreMer and *Lmna* floxed mice were crossed to obtain mice hemizygous for αMHC-MerCreMer and homozygous for *Lmna* floxed (*Lmna*$^{fl/fl}$). αMHC-MerCreMer hemizygous expressing wild-type *Lmna* (*Lmna*$^{+/+}$) littermates served as controls (*Lmna*-cWT). To induce lamin A/C depletion in cardiomyocytes, tamoxifen (Cayman chemicals cat#13258) was dissolved in sunflower seed oil (Sigma cat# 88921) to a concentration of 30 mg/kg and injected intraperitoneally at 9-10 weeks of age for five consecutive days, followed by a one-week-long washout period. Vehicle-only injections served as additional controls. For tissue collection, mice were anesthetized at the appropriate timepoints using Isoflurane. Immediately following cervical dislocation, hearts were harvested, washed with ice cold 1X Phosphate Buffer Saline (1X PBS), and processed for downstream analysis. All experiments, including breeding, maintenance, and euthanasia of animals, were performed in accordance with relevant guidelines and ethical regulations approved by the Cornell University Institutional Animal Care and Use Committee (IACUC), protocol 2011–0099. Genotyping was performed by PCR using genomic DNA isolated from tail clippings following the protocol and sequencing primers suggested by JAX. Mice were housed in a disease-free barrier facility with 12/12 hr light/dark cycles.

Cardiac function. Mice were anesthetized with 2% isoflurane and placed on a stereotactic heated scanning base (37°C) attached to an electrocardiographic monitor. Left ventricular function was determined with a Vevo 2100 imaging system (VisualSonics)

equipped with a MS550D transducer (22–55 MHz). Ejection fraction (EF%), fraction shortening (FS%), left ventricle diameter during systole (mm) and volume during systole (mm) were measured for at least five cardiac cycles using AM mode images. The average heart rate for all studied animals was 461 +/- 24 beats per minute (BPM). Analysis was performed using the AutoLV Analysis Software (VisualSonics) and conducted by observers blinded to the mouse genotype and/or treatment groups.

Immunofluorescence and histology of mouse tissues. Immediately following tissue collection, hearts were washed with 1X PBS and fixed in 4% paraformaldehyde (diluted in 1X PBS) at 4°C overnight. Samples were stored for up to one week in 70% ethanol (diluted in 1X PBS) at 4°C before being embedded in paraffin, sectioned, and stained with Masson's Trichrome using standard methods at the Animal Health Diagnostic center (Collage of Veterinary Medicine, Cornell University). For immunofluorescence analysis, samples were washed with PBS and flash frozen in Tissue-Tek® O.C.T. Compound (Sakura, #4583) in an ethanol bath, followed by storage at –70°C. Frozen tissue blocks were cryosectioned using an Epredia™ Microm HM525 NX Cryostat (SN: S20020277) to a thickness of 5 µm, mounted on 25 × 75 × 1.0 mm Superfrost Plus Microscope slides (Fisherbrand® #12-55015) and left to air-dry for 1 hour. Samples were stored at –20°C until processed for immunofluorescence staining and imaging. Prior to staining, slides containing tissue were equilibrated to room temperature and rehydrated with 1X PBS for 5 minutes. When using primary antibodies raised in mice, tissues were initially blocked with M.O.M® (Mouse on Mouse) Blocking Reagent (Vector laboratories, Cat# MKB-2213-1, diluted 1:20 in 1X PBS) for 1 hour at room temperature, followed by additional blocking and permeabilization with a solution of 3% BSA, 5% filtered horse serum in PBS-T (0.05% Triton-X 100 and 0.03% Tween (Sigma) in 1X PBS) for 1 hour at room temperature. Tissues were then incubated with primary antibodies diluted in blocking solution at 4˚C overnight. The following primary antibodies were used for this study: pcm1, Santa Cruz sc398365, 1:50 dilution; pcm1, Sigma HPA023370, 1:500; Lamin A/C (E-1), Santa Cruz sc376248, 1:100; lamin A, Sigma MAB3540, 1:100; CD68 (E3O7V), Cell Signaling 97778T, 1:400; 53BP1, Novis NB100-304, 1:200. Samples were washed with PBS-T and incubated for 1 hour at room temperature with AlexaFluor secondary antibodies (Invitrogen, 1:300 dilution) and Hoechst Nucleic Acid Stains (ThermoFisher 62249, 1:1000) in PBS-T.

Bulk RNA sequencing (RNA-seq). Left ventricle free wall tissues (excluding the atria and septum) were harvested at the appropriate timepoints, flash frozen in liquid nitrogen, and stored at –70°C until RNA was extracted. Frozen tissue was placed in an Eppendorf tube containing one metal bead and 500 µl of TRIzol® reagent (Invitrogen, #15596018). Tissues were homogenized for five 3-minute cycles of 30 shakes/sec using a TissueLyser II (Qiagen) and transferred to an RNase free microfuge tube (Ambion, Cat #AM12400). 1:5 chloroform was added and mixed by shaking, followed by a 5-minute centrifugation at 4°C 14,000 rpm. The clear supernatant was carefully transferred to a gDNA eliminator spin column (RNeasy Plus Mini Kit, Qiagen, #74136) and RNA purification was performed according to manufacturer instruction. RNA quality control was performed by the Cornell Genomics core facility with a fragment analyzer (Agilent) to assess RNA integrity (RIN); RNA concentrations were quantified by Nanodrop (ThermoFisher Scientific). To generate

cDNA directional RNA-seq libraries (New England Biolabs, #E7760), 1 µg of total RNA sample (with RIN ≥ 7) was enriched for mRNA (New England Biolabs, #E7490) for each condition. Each sample received a unique barcode for downstream multiplexing. cDNA library size distribution and concentrations were again assessed by fragment analyzer and Qubit. Final libraries were pooled in equimolar concentrations, 12 samples per lane, and sequenced on a NextSeq 500 (Illumina) with a 75 bp kit by the Cornell Genomics core facility.

Bulk RNA-seq analysis. We used STAR software[31] (version 2.7.3a) to generate a genome for read alignment using the GRCm38/mm10 (Ensembl release 102) mouse FASTA and GTF files. Fastq files were then aligned to the STAR genome using default parameter settings, resulting in a uniquely mapped read alignment ≥ 85%. Gene-level quantification was performed using the featureCounts function from Subread[32] (version 2.0.2), with parameters -s 2 (for directional RNA-seq libraries) and the GENCODE GTF annotation file (vM23), to generate a count matrix using all samples. PCA and distance correlation matrix analyses were performed to identify and remove outliers (samples 3 and 19) before downstream processing. Differential gene expression (DEG) analysis was performed in R (v4.1.1) by applying DESeq2[33] (v1.34.0) to the input count matrix. The design formula "~genotype*timepoint", where genotypes were either *Lmna*-cKO or corresponding controls, and timepoints were either 11- or 25-days post-injection (dpi), was used. The ashr[34] shrinkage estimator was applied to all DEG results. DEGs were defined as genes with |log2-fold change| ≥ 1, baseMean ≥ 10, and p-adj < 0.05.

Computation of emerging DEGs (eDEGs). We first filtered DEG analysis results for *Lmna*-cKO versus *Lmna*-cWT samples at 11- and 25-dpi, based on meeting a significance threshold of *p*-adj < 0.05. All 11-dpi genes that met the significance threshold (1,405 genes) were retained for downstream analysis, irrespective of fold-change (FC). The 25-dpi significance-filtered genes were further refined using a |log2 FC| ≥ 1 threshold (2,951 genes), thus meeting DEG requirements outlined in the "Bulk RNA-seq analysis" section. The 1,405 11-dpi genes and 2,951 25-dpi DEGs were compared, revealing 508 matches between the two gene sets. Of these 508 genes, 496 genes were found to have a FC directionally (up- or down-regulated) that matched at both early (11-dpi) and late (25-dpi) timepoints and were termed eDEGs.

Single-nucleus RNA sequencing (snRNA-seq) and analysis. Left ventricle free wall tissues (5-6 left ventricles per experimental group) were harvested at the appropriate timepoints, flash frozen in liquid nitrogen, and sent to SingulOmics (Bronx, NY, USA) for processing. There, nuclei were isolated from frozen samples and used to construct 3' single cell gene expression libraries (Next GEM v3.1) using the 10X Genomics Chromium system. Libraries were sequenced with ≈200 million PE150 reads per sample on Illumina NovaSeq 6000. Sequencing reads, including introns, were then aligned with the mouse reference genome (mm10/GENCODE vM23/Ensembl 98) using Cell Ranger[35] (v7.0.1). The Debris Identification using Expectation Maximization (DIEM) algorithm[36] was applied to remove background, keeping barcodes with debris scores < 0.5, UMI count >800, and number of features (genes) > 250. The resulting dataset was composed of 22,043 total nuclei (5,052 11-dpi and 5,939 25-dpi in *Lmna*-cKO; 6,300 11-dpi and 4,752 25-dpi *Lmna*-

cWT), before downstream filtering. snRNA-seq sample outputs from Cell Ranger were then loaded into R (v4.1.1) and individually subjected to the standard Seurat (v5.0.1) pipeline and sctransform. All samples were processed for ambient RNA (SoupX[37], v1.6.2) and doublet (DoubletFinder[38], v2.0.3) removal individually. Sample integration was performed with the integrated object subjected to the same standard Seurat pipeline as above, with a cluster resolution of 0.5. To annotate individual clusters with cell types, mouse genes were first converted to human orthologous genes. The converted snRNA-seq dataset was then compared to the Azimuth human heart reference map[39-41] to assess prediction mapping scores[42]. Cells with high-confidence annotations (prediction scores > 0.75) were used to determine cell types in each identified cluster. To identify cell type-specific subclusters, each cell type cluster was subjected to the standard Seurat (v5.0.1) pipeline and sctransform with unique cluster resolution (0.9 forcardiomyocyte, 0.7 for myeloid cells, 0.5 for fibroblasts, 0.6 for B cells, and 0.8 for NK/T cells). DEG analyses were performed for each cell type cluster using Seurat's FindMarkers function: 1) *Lmna*-cKO vs. *Lmna*-cWT at 11- and 25-dpi across all cells in the cluster irrespective of subcluster, and 2) each subcluster vs. all other subclusters irrespective of experimental condition. Genes were required to meet a threshold of $|\log2\ FC| \geq 0.1$, p-adj < 0.05, and for the fraction of cells expressing the gene to be ≥ 0.01 for at least one of the two queried populations.

Deconvolution analysis. Deconvolution was performed on the BayesPrism[43] (version 1.0) gateway web interface and server[44]. An RDS file of the Seurat object containing the integrated heart snRNA-seq dataset, a metadata file of cell type annotations for all captured nuclei, and the count matrix from the bulk RNA-seq dataset were submitted as input. The resulting BayesPrism R object was used to extract count matrices deconvolved for each cell type. A DEG analysis comparing *Lmna*-cKO vs. *Lmna*-cWT samples was performed on each cell type-deconvolved count matrix using the same DESeq2 pipeline employed in the bulk RNA-seq dataset. In addition, cell type fractions of transcriptional representation in the bulk RNA-seq dataset were extracted from BayesPrism's final theta parameter.

Cell-cell interaction prediction. Cell-cell communication prediction was determined using CellChat[45] (version 2.1.1). The CellChat algorithm computes the strength of specific predicted cell-cell interactions, quantified as the sum of the communication probability of all ligand-receptor interactions, in each experimental condition[46]. CellChat objects were generated using Seurat snRNA-seq objects for each condition individually and processed using the default pipeline to identify enriched ligand-receptor interactions between all cell types. CellChat objects were then merged based on timepoints to perform a comparative analysis of cell-cell communication between *Lmna*-cKO and *Lmna*-cWT samples over time.

Functional enrichment analysis. DEGs and eDEGs Log2-fold change-ranked gene symbol lists were submitted to Gene Set Enrichment Analysis[47, 48] (GSEA, version 4.2.3), Metascape[49] (version 3.5.20240101), StringDB[50] (version 12.0), and QIAGEN's Ingenuity Pathway Analysis (IPA) software[51] (version 111725566) for functional enrichment analysis. All analyses used the gene ontology[52, 53] (GO) biological processes and

Reactome[54] (version 3.6) databases for enrichment. To perform GSEA, gene lists were first remapped to human orthologues and then tested for enrichment in the human GO biological processes database using default parameters. Finally, results from GSEA were filtered using the default significance threshold (FDR q-val < 0.25). To perform comparative analyses between gene sets, multiple gene lists were provided simultaneously to Metascape using default parameters. StringDB was used to identify protein-protein interaction (PPI) networks made up of only high confidence interactions (>0.7 interaction score) and involving more than two proteins. Comparative analyses of predicted upstream regulators between different gene sets were performed using IPA, assuming a |z-score| > 2 and *p*-value < 0.05 as predictive of regulator activation or inhibition.

Data availability. The bulk RNA-seq and snRNA-seq datasets generated from isolated left ventricle free wall tissue samples and used to support the conclusions in this article are limited to reviewers and journal editors for the preprint version of the manuscript. All data will be made publicly available in the GEO repository following peer review and publication.

Statistical analysis. Animals were randomly assigned to treatment groups, and experiments were conducted blinded to treatment and genotype. Since Cre expressed in the heart can be cardiotoxic at high tamoxifen doses, experiments used only low tamoxifen doses (30 mg/kg/day). Furthermore, for maximum stringency, comparisons are focused on groups in which all mice express the MCM transgene but differ in the status of the floxed *Lmna* gene. Tissues isolated from individual mice were counted as a single replicate (unless otherwise specified). Since the bulk-RNA sequencing data did not show any sex difference, male and female mice were combined for downstream transcriptomic analysis. Survival curves were generated using the Kaplan–Meier method and differences in survival tested with a Breslow test. For results that follow a Gaussian distribution, the mean and standard error of the mean (SEM) were calculated; comparison between two groups used t-tests; ANOVA with Tukey or Dunnett post-analysis was used to test for statistical significance between more than two experimental groups. Data linearity was determined using Pearson correlation coefficients and significance calculated using the R package ggpubr[55].

Results

Cardiomyocyte-specific depletion of lamin A/C in adult mice causes severe dilated cardiomyopathy

To determine the cardiac effects of *Lmna* deletion without confounding effects from other cell types or adaptation during development, we generated mice with inducible, cardiomyocyte-specific lamin A/C depletion (*Lmna*-cKO). Tamoxifen treatment of adult *Lmna*-cKO mice (Figure 1A) led to ≈50-70% reduced lamin A levels in cardiomyocytes by 11 days post injection (dpi), compared to tamoxifen treated littermate controls (*Lmna*-cWT) that expressed the MCM recombinase but lacked the floxed *Lmna* alleles (Figure 1B-C). Lamin A levels in non-cardiomyocytes were not affected (Figure 1B). The incomplete lamin depletion in cardiomyocytes is consistent with other studies using similar cardiomyocyte-specific mouse models[28] and is likely due to the long half-life of lamin A/C in post-mitotic cells[56]. Immunofluorescence staining for lamin A/C showed a similar trend, albeit with less substantial lamin depletion, likely due to poorer antibody labeling (Suppl. Fig. S1A-B). Since the lamin A antibody produced better labeling in cardiac tissue sections, and results obtained with this antibody matched those of a recent study in the same genetic model[28], subsequent results are based on lamin A staining.

Despite the incomplete depletion of lamin A/C, tamoxifen treated *Lmna*-cKO mice rapidly developed severe DCM, which was not observed in the *Lmna*-cWT controls (Figure 1D-E; Suppl. Figure S1E-F). Histological analysis demonstrated increased cardiac fibrosis and thinning of the ventricular walls of *Lmna*-cKO hearts already at 11-dpi, followed by substantial left ventricular enlargement of *Lmna*-cKO hearts by 25-dpi, compared to *Lmna*-cWT littermate controls (Figure 1D-F; Suppl. Figure S1E-F). Echocardiographic analysis revealed a reduction in cardiac function in tamoxifen treated *Lmna*-cKO mice at 11-dpi that progressively worsened by 25-dpi (Figure 1G-H; Suppl. Figure S1G-J).

Consistent with the severely impaired cardiac function, tamoxifen treated *Lmna*-cKO mice had dramatically reduced survival compared to *Lmna*-cWT controls (Figure 1I) and vehicle-only treated *Lmna*-cKO controls (Suppl. Figure S1D). Male *Lmna*-cKO mice died on average by 22-dpi, whereas female *Lmna*-cKO mice lived until 34-dpi. In contrast, tamoxifen-treated *Lmna*-cWT controls did not exhibit premature death (Fig. 1I), indicating the absence of cardiotoxic effects from the Cre recombinase at the tamoxifen dose administered here. Intriguingly, whereas other striated laminopathy mouse models typically show external signs of disease such as loss of body weight and reduced motility [57], *Lmna*-cKO mice died suddenly following lamin A/C depletion, without preceding weight loss (Figure 1J) or other external indications such as impaired mobility. Collectively, these findings indicate that even partial reduction in lamin A/C protein levels in cardiomyocytes results in severe and rapid onset of DCM, corresponding with previous reports of reduced lamin A/C levels in cardiomyocytes of *LMNA*-DCM patients, regardless of the underlying mutation classification[14, 29, 58, 59].

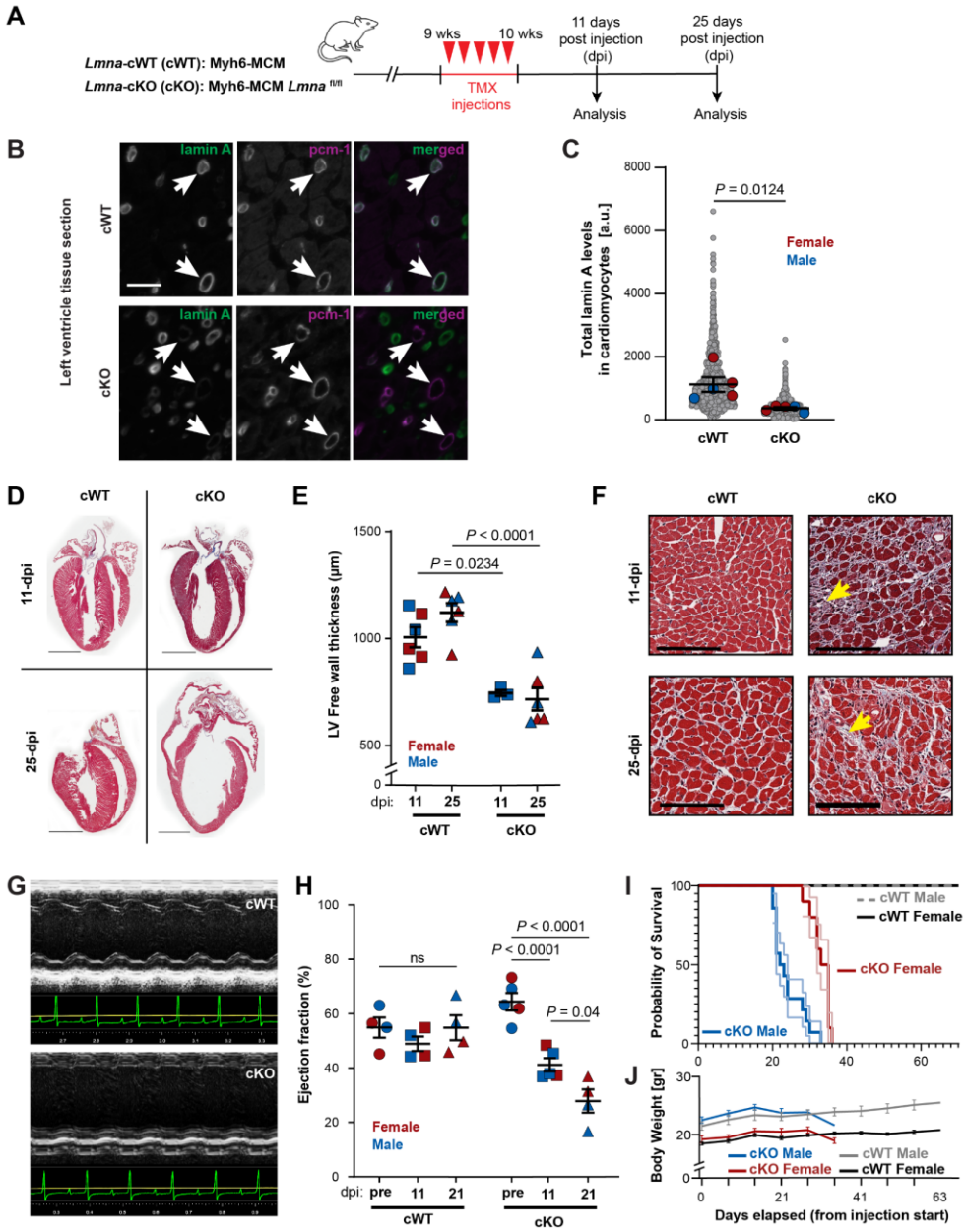

Figure 1: Cardiac specific lamin A depletion leads to dilated cardiomyopathy in adult mice. (A) *Lmna*-cKO (cKO) and *Lmna*-cWT (cWT) mice were injected with 30 mg/kg tamoxifen for 5 consecutive days, starting at 9-10 weeks of age. Following a wash out period, cardiac tissues were collected for analysis at two time points: 11 days post injection (dpi), signifying a stage where DCM has not fully developed, and 21-25 dpi, in which disease is already well pronounced. Functional cardiac measurements (echocardiography) were performed at the same time points. **(B)** Representative immunofluorescence images of cardiac tissues from *Lmna*-cKO (top) and *Lmna*-cWT (bottom) mice stained for lamin A (green) and Pcm-1 (magenta), a cardiomyocyte-specific marker. Scale bar 20 µm. Arrows indicate representative cardiomyocytes. **(C)** Quantification of total lamin A levels in cardiomyocytes showing a significant depletion of lamin A levels in *Lmna*-cKO mice. Larger colored circles represent average values for individual male (blue) or female (red) mice. Smaller gray circles represent individual

cardiomyocytes. *N* = 5 animals per genotype. Statistics are based on the mean values of individual animals. **(D)** Representative images of whole hearts stained with Masson's trichrome showing progressive thinning of the left ventricle free wall and enlargement of *Lmna*-cKO hearts. Scale bar 2 mm. **(E)** Quantification shows significant thinning of left ventricle free wall thickness in *Lmna*-cKO mice compared to *Lmna*-cWT at 11-dpi and 25-dpi. **(F)** Masson's trichrome staining of heart sections. Yellow arrows indicate collagen deposition in *Lmna*-cKO hearts at both early (11-dpi) and late (25-dpi). Scale bar: 100 µm. **(G)** Representative images of M-mode echocardiography of *Lmna*-cWT (top) and *Lmna*-cKO (bottom) mice performed at 25-dpi. **(H)** Left ventricular ejection fraction (EF), given as percent, measured by echocardiography. Symbols represent %EF of individual mice. Red symbols denoting female mice, blue male mice. Error bars represent mean ± S.E.M. **(I)** Kaplan-Meier survival plot for *Lmna*-cWT mice (*N* = 14 males and 11 females) and *Lmna*-cKO mice (*N* = 14 males and 10 females). **(J)** Body weight measurements performed during the course of the survival study on the mice in panel (I) before (0) and after (day-dpi) tamoxifen (TMX) injections.

Identification of early *LMNA*-DCM disease-driving genes

To identify transcriptional changes resulting from cardiac-specific *Lmna* deletion in mouse hearts over the course of the disease progression, we performed bulk and single-nucleus RNA sequencing (RNA-seq and snRNA-seq, respectively) of left ventricular free wall tissue samples of tamoxifen-treated *Lmna*-cKO and *Lmna*-cWT controls at 11- and 25-dpi (Figure 2A). For our initial analysis, we focused on bulk RNA-seq results, given the higher sensitivity and gene coverage compared to snRNA-seq. Since we did not detect any sex-specific differences at the transcriptional level (Suppl. Figure S2A), we combined data from male and female mice for subsequent analyses. Tamoxifen-treated *Lmna*-cKO cardiac tissues had substantially decreased *Lmna* expression compared to *Lmna*-cWT controls at 11- and 25-dpi (Suppl. Figure S2B), consistent with our immunofluorescence analysis (Figure 1B-C). Principal component analysis (PCA) of RNA-seq data revealed a subtle segregation at 11-dpi between *Lmna*-cKO and *Lmna*-cWT controls, which grew into distinct genotypic clusters by 25-dpi (Figure 2B). This increase in transcriptomic divergence over time was further highlighted by the number of differentially expressed genes (DEGs) identified between *Lmna*-cKO and *Lmna*-cWT samples at corresponding timepoints, which increased from 86 DEGs at 11-dpi to 2,951 DEGs at 25-dpi (Figure 2C-D). Most DEGs showed increased expression in the tamoxifen-treated *Lmna*-cKO mice compared to *Lmna*-cWT controls, with upregulated DEGs representing 95% (11-dpi) and 67% of DEGs (25-dpi), respectively (Figure 2D). These results suggest that *Lmna*-cKO hearts have a pronounced activation of transcriptional programs, with the extent of activation increasing over the course of disease progression.

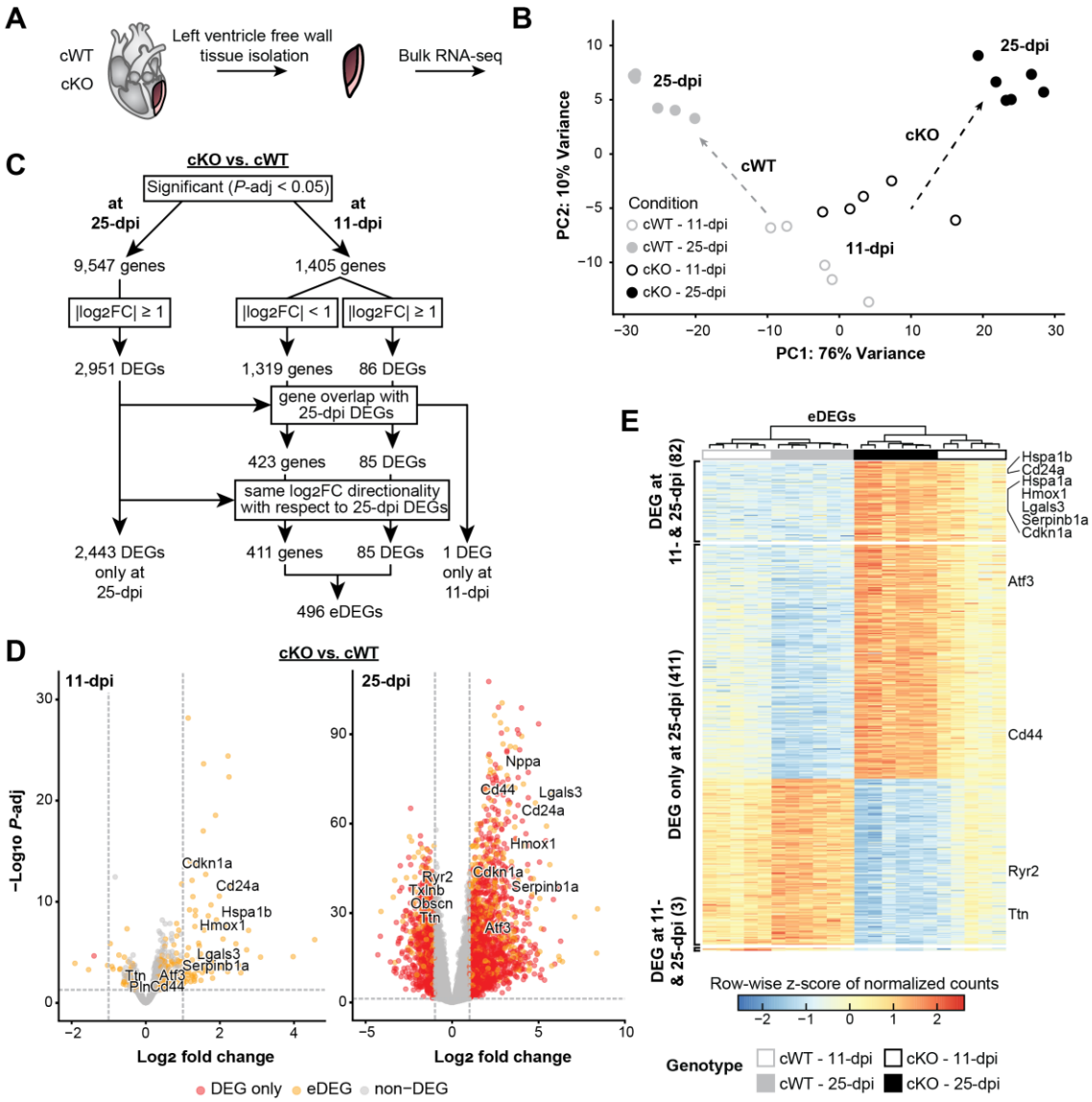

Figure 2: Bulk RNA sequencing identified early disease-driving genes. (A) Schematic depicting the experimental setup for bulk RNA sequencing (RNA-seq), including experimental conditions (*Lmna*-cKO (cKO) and *Lmna*-cWT (cWT)) and representation of the isolated heart tissue. **(B)** Principal components analysis (PCA) plot of bulk RNA-seq sample from all experimental conditions. Dashed lines and arrows indicate direction of movement of *Lmna*-cKO and *Lmna*-cWT genotypes from 11- to 25-dpi. **(C)** Flow chart demonstrating the steps to identify emerging differentially expressed genes (eDEGs), based on log2-fold change (Log2FC) and adjusted *P*-values (*P*-adj) generated when comparing the gene expression between *Lmna*-cKO and *Lmna*-cWT samples at each timepoint. **(D)** Volcano plot of the DEG analysis performed on bulk RNA-seq data comparing *Lmna*-cKO and *Lmna*-cWT samples at 11- (left) and 25-dpi (right). Genes meeting DEG requirements (*P*-adj < 0.05 and |Log2FC ≥ 1|) but not defined as eDEG are represented in red, eDEGs are shown in orange, and genes not meeting either DEG or eDEG requirements are shown in gray. Select genes identified throughout the study are highlighted. **(E)** Heatmap of row-wise z-score normalized read counts for eDEGs. Rows are separated based on meeting DEG requirements at both timepoints (85 genes, top and

bottom sections) or meeting DEG requirements at 25-dpi and significant difference by 11-dpi (411 genes, middle section). Columns, indicating individual samples, were sorted using unbiased hierarchical clustering, with experimental conditions denoted below by color. Select genes identified throughout the study are highlighted.

We hypothesized that some early changes in gene expression may be too subtle to meet our stringent criteria for DEGs, i.e., more than 2-fold change (FC) in expression (|log2-FC| ≥ 1), yet still contribute to disease pathogenesis. Therefore, we developed an analysis pipeline to detect genes that already showed statistically significant changes in expression (i.e., *p*-adj < 0.05) at 11-dpi, but only exceeded the log2-FC threshold at the 25-dpi timepoint (Figure 2C). Based on these criteria, we identified 423 genes with altered expression at 11-dpi, in addition to the 85 DEGs identified at 11-dpi that were also found at the 25-dpi timepoint. Of these 508 combined genes that overlapped with 25-dpi DEGs (i.e., 423 plus 85 genes), 496 genes (98%) had the same directional change (i.e., either up- or down-regulated) at both early (11-dpi) and late (25-dpi) timepoints. We termed these 496 genes, which represent genes that are already significantly misregulated in early disease, 'emerging DEGs' (eDEGs) and hypothesized that these eDEGs play crucial roles in *LMNA*-DCM pathogenesis. Most of the eDEGs were upregulated (322 up versus 174 down), with larger fold-changes of the upregulated eDEGs compared to the downregulated eDEGs (Figure 2D-E). Furthermore, hierarchical clustering of samples based on eDEG expression created distinct separation based on genotype and timepoint (Figure 2E). Together, these results demonstrate that our methodology enables the detection of early disease contributing genes and their underlying processes, which may have been overlooked using previous standard gene thresholding methods. Therefore, the remainder of the analyses performed in this study focuses on the newly identified eDEGs.

Lamin A/C-depleted hearts have increased DNA damage and activation of cytosolic DNA and DNA damage response pathways

To identify potential disease driving biological processes mediated by the eDEGs, we performed comparative Gene Ontology (GO) analysis between the eDEGs and the DEGs identified at 25-dpi (Figure 3A). The top 10 GO cluster terms overrepresented among these two gene sets included several terms related to cardiac muscle organization and contraction, consistent with the impaired cardiac function and fibrosis present in *Lmna*-cKO hearts already at 11-dpi (Figure 1F-H). The analysis further confirmed several previously identified alterations in lamin A/C deficient cells, such as increased MAPK activation[60] and autophagy[61]. Additionally, the GO cluster analysis showed a clear enrichment of eDEGs associated with apoptosis and other processes mediated by DNA damage. These eDEGs had a higher degree of enrichment and significance in comparison to 25-dpi DEGs (Figure 3A, bottom), indicating an important role in early disease development. Previous reports have shown evidence of nuclear envelope damage in clinical patient samples and the presence of chromatin protrusions and nuclear envelope ruptures in various mouse models of striated laminopathies at an early disease stage [25, 28, 62-70]. Such loss of nuclear envelope integrity can result in DNA protruding into

the cytoplasm and influx of cytoplasmic nucleases into the nucleus, causing an increase in DNA damage and the activation of DNA damage repair mechanisms and immune response[21, 28, 71-73]. Consistent with this idea and a recent report showing extensive nuclear envelope rupture in a similar *Lmna*-cKO model[28], many of the top 25 upstream regulators of the eDEGs predicted by Ingenuity Pathway Analysis (IPA) are components of the STING cytosolic DNA sensing pathway, including Sting1, Irf3, Irf7, Myd88, NF-κB (*NFKB*), and several cytokines (Table 1). The predicted upstream regulators further contained several molecules involved in DNA damage responses, including *Trp53* (*TP53*), which encodes p53, and the TREX1 nuclease that degrades cytoplasmic DNA and has been implicated in DNA damage following nuclear envelope rupture[71].

To validate these findings and to assess the timing and extent of DNA damage in the *Lmna*-cKO cardiomyocytes, we quantified the presence of 53BP1 foci, a common marker of double-strand DNA damage, in hearts of tamoxifen treated *Lmna*-cKO and *Lmna*-cWT mice. *Lmna*-cKO hearts had an increased fraction of cardiomyocytes with 53BP1 foci at 11-dpi (Figure 3B-C); the fraction remained elevated at 25-dpi but did not reach statistical significance (P = 0.138). Across all cardiac samples, the fraction of cardiomyocytes positive for 53BP1 inversely correlated with the averaged lamin A protein levels in cardiomyocytes (Fig. 3D), further supporting a strong link between reduced lamin A levels and increased DNA damage early in *LMNA*-DCM pathology.

DNA damage and cytosolic DNA mediated STING and NF-κB activation can lead to increased expression of pro-inflammatory cytokines and Type I interferons such as INF-α [74]. Furthermore, advanced *LMNA*-DCM is often characterized by inflammation and immune activation. Consistent with these findings, our analysis of common GO cluster terms among the eDEGs and 25-dpi DEGs revealed an enrichment for immune responses and inflammation (Figure 3A, top), including terms related to “cytoplasmic pattern recognition receptor signaling”, which includes cytosolic DNA sensing pathways such as cGAS/STING. Furthermore, GO cluster results were particularly associated with innate immunity. To confirm these transcriptomics findings, we quantified the presence of macrophages in cardiac tissues using the common macrophage/monocyte marker CD68. *Lmna*-cKO left ventricular samples had an increased prevalence of macrophages compared to *Lmna*-cWT controls, based on both the intensity of the CD68 antibody signal and the CD68-positive area, starting at 11-dpi and increasing further at 25-dpi (Figure 3E-F). Unlike DNA damage, which reached its highest levels at 11-dpi, immune cell infiltration peaked at 25-dpi (Figure 3E-F). Together, these findings suggest that lamin A/C depletion in adult cardiomyocytes results in accumulation of DNA damage early in disease, potentially due to ruptures of the weakened nuclear envelope of *Lmna*-cKO cardiomyocytes, promoting the activation of cytosolic DNA sensing pathways and ultimately the increased recruitment of innate immune cells.

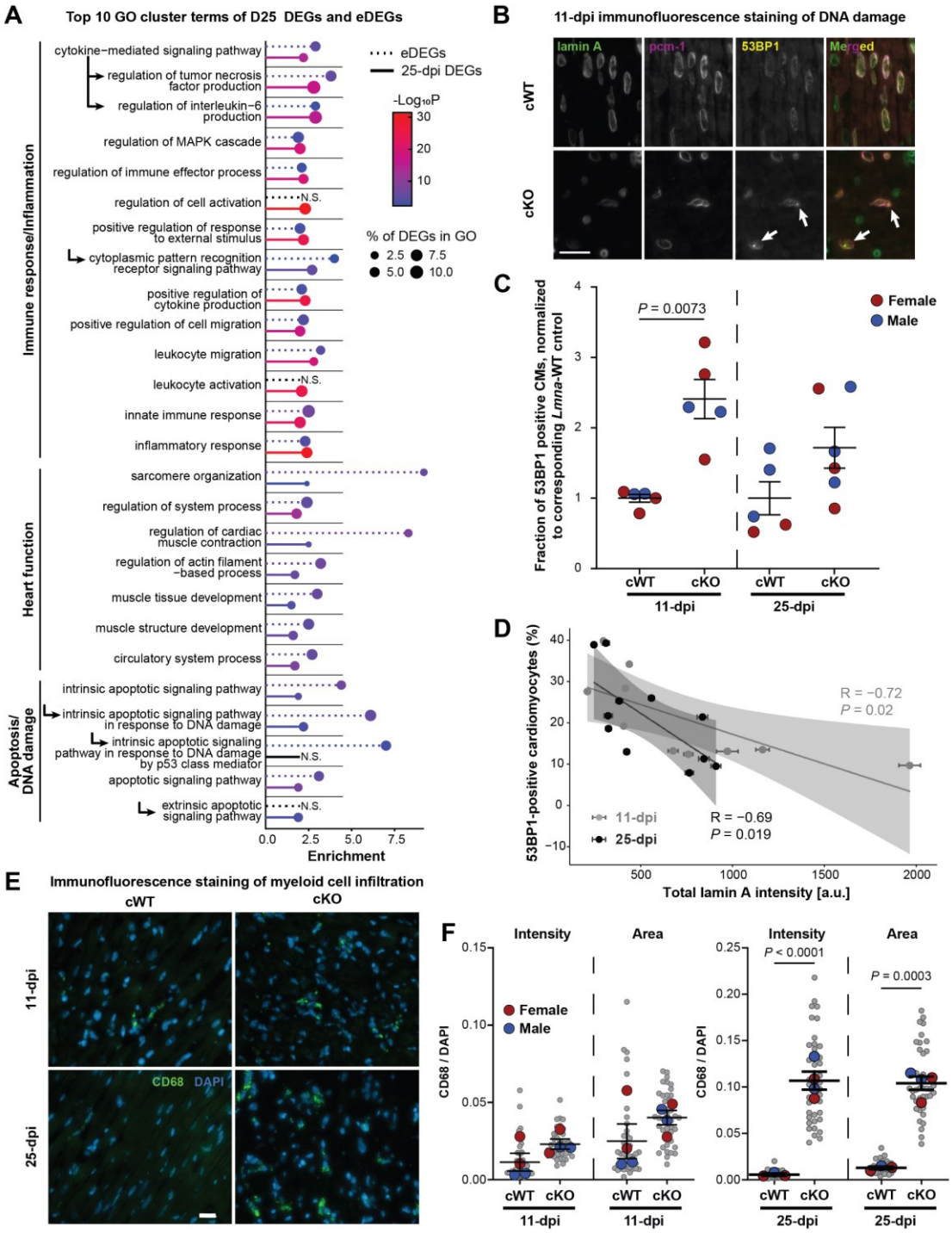

Figure 3: DNA damage preceded immune infiltration in *LMNA*-DCM hearts. (A) Lollipop plot of top 10 Gene Ontology (GO) cluster terms enrichment among emerging differentially expressed genes (eDEGs, dashed line) and 25-dpi DEGs (continuous line). Arrows indicate child terms present below their respective parent term. **(B)** Representative images of cardiac tissue sections from *Lmna*-cWT (top) and *Lmna*-cKO (bottom) hearts at 11-dpi stained with antibodies against lamin A (green), the cardiomyocyte specific marker pcm-1 (magenta), and the dsDNA damage marker 53BP1 (yellow). Scale bar 20 µm.

Arrows indicate representative cardiomyocytes positive for 53BP1. **(C)** Quantification of percentage of 53BP1 positive cardiomyocyte normalized to age-matched *Lmna*-cWT showing significantly more DNA damage in 11-dpi *Lmna*-cKO cardiomyocytes, and a trend towards increased DNA damage at 25-dpi (P = 0.138) N = 5-6 mice/group. **(D)** Inverse correlation between the percentage of cardiomyocytes showing evidence of DNA damage (53BP1 positive) and averaged cardiomyocyte total lamin A levels at both 11-dpi (gray) and 25-dpi (black). **(E)** Representative images of cardiac tissue sectioned from *Lmna*-cWT (left) and *Lmna*-cKO (right) hearts stained with antibodies against CD68 (green), a macrophage marker, and DAPI (blue), to stain DNA. Scale bar 20 µm. **(F)** Quantification of CD68 intensity (normalized to DAPI) and area in *Lmna*-cWT and *Lmna*-cKO cardiac tissue sectioned at 11-dpi (left) and 25-dpi (right). Gray dots represent individual fields of view images (10/mouse), large dots represent the average values for each individual mouse analyzed. Statistics are based on the mean values of individual animals. N = 3-4 mice/group.

Two cardiomyocyte subclusters predominantly account for decreased heart function and increased apoptosis in *Lmna*-cKO hearts

Since bulk RNA-seq cannot distinguish the individual transcriptional contribution of different cell types to the overall response, we subsequently focused on the snRNA-seq analysis of left ventricle free wall tissue isolated at 11- and 25-dpi from tamoxifen treated *Lmna*-cKO mice and *Lmna*-cWT controls. For these experiments, hearts from five to six mice were pooled for each condition to increase robustness of results, yielding a total of >22,000 nuclei (≈5,000 nuclei per sample) for sequencing. To obtain a comprehensive view of the effect of cardiomyocyte-specific lamin A/C depletion on specific ventricular cell populations, we combined and harmonized the transcriptomes of snRNA-seq datasets for each experimental condition into a single dataset, enabling us to match shared cell types and accurately compare the gene expression of individual nuclei across timepoints and genotypes (Figure 4A). Cell type annotation, based on comparison to a reference database for cardiac tissue[39-41], identified many of the expected cell types previously found in left ventricular tissue[75], including cardiomyocytes, immune cells, fibroblasts, and endothelial cells (Figure 4B).

We first focused specifically on the cardiomyocyte population in the snRNA-seq dataset, given that this cell population contains the *Lmna* deletion and is directly involved in *LMNA*-DCM. We identified five distinct cardiomyocyte subclusters (Figure 4C), two of which (CM3 and CM5) were almost exclusive to *Lmna*-cKO hearts (Figure 4C-D) and progressively increased in size over the course of disease progression from 67 to 267 nuclei (out of ≈800 total cardiomyocyte nuclei) at 11- and 25-dpi, respectively. We then identified genes that were uniquely differentially expressed within distinct subclusters in comparison to the rest of the cardiomyocyte population. Gene set enrichment analysis (GSEA) of DEGs unique to CM3 and CM5 established that these subclusters specifically correlated with decreased heart function, through the downregulation of contraction and conduction processes, and the upregulation of processes associated with DCM, i.e., proteolysis, autophagy, and apoptosis[19, 61, 76] (Figure 4E). To determine the transcriptional contribution of DEGs represented in subclusters CM3 and CM5 in driving DCM pathogenesis, we further compared them to the eDEGs identified in the bulk RNA-seq

analysis. The DEGs showed strong overlap with eDEGs and shared the same directionality in their change of expression (Figure 4F). We additionally confirmed that population-wide 11- and 25-dpi DEGs (*Lmna*-cKO vs. *Lmna*-cWT) overlap with the eDEGs (Figure 4F) was largely driven by subcluster CM3 and CM5 DEGs (Figure S3A). These results suggest that we have identified the transcriptional profile of pathogenic cardiomyocytes associated with the eDEGs.

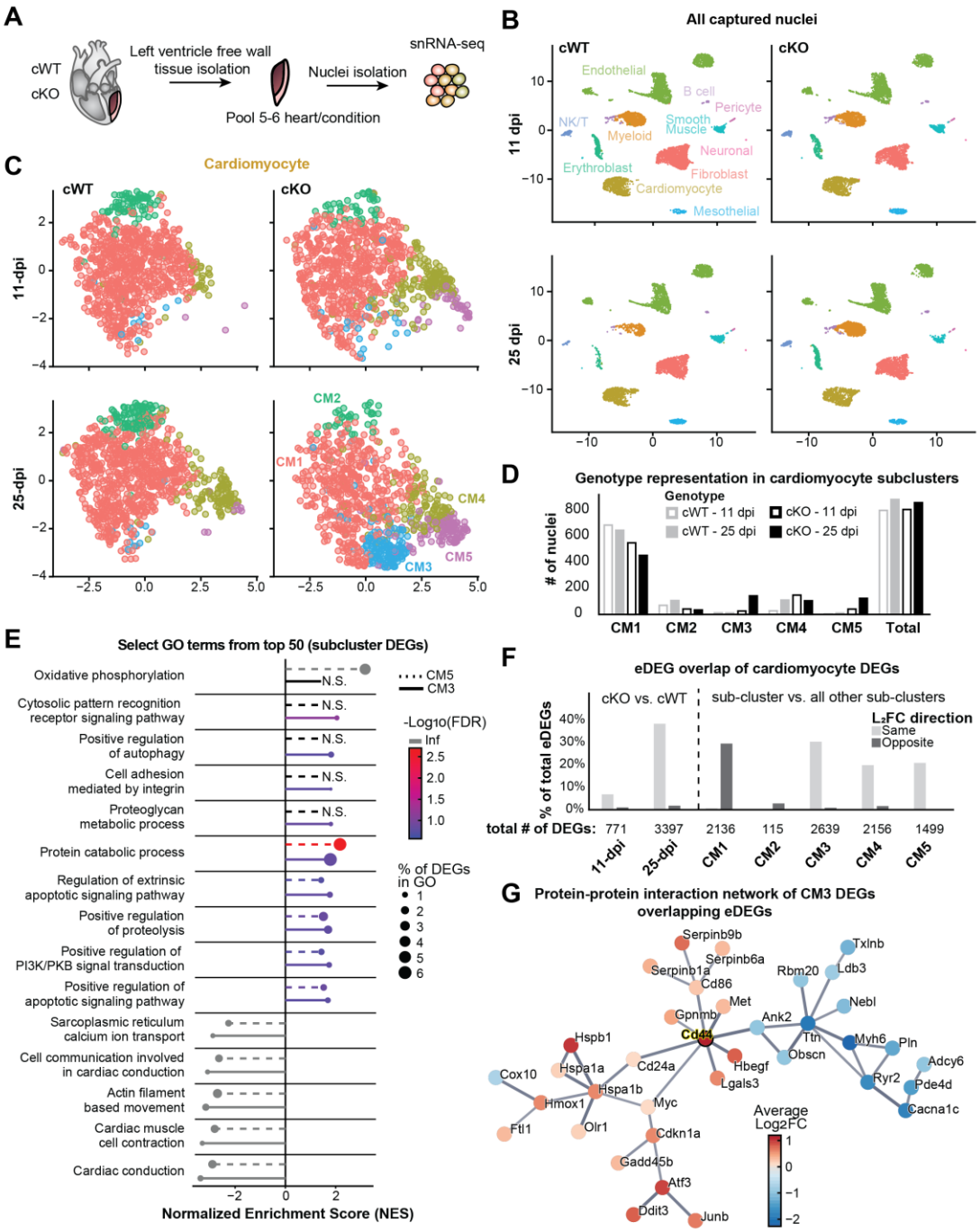

Figure 4: *Lmna*-cKO-specific cardiomyocyte subclusters predominantly accounted for early disease-driving genes involved in decreased heart function and increased apoptosis. (A) Schematic depiction of the experimental setup for single nucleus RNA-seq (snRNA-seq), including experimental conditions (*Lmna*-cKO (cKO) and *Lmna*-cWT (cWT)) and a representation of the isolated heart tissue giving rise to distinguishable cell types. UMAP plots of **(B)** integrated snRNA-seq nuclei and **(C)** cardiomyocyte subclusters, across genotype (left and right) and timepoint (top and bottom). Individual colors represent unique **(B)** cell type clusters or **(C)** cardiomyocyte-specific subclusters identified (CM1-5). **(D)** Barchart of the number of nuclei captured in each genotype within individual cardiomyocyte subclusters and in total. **(E)** Lolliplot plot of select top 50 Gene Ontology (GO) terms enrichment in subclusters CM3 (continuous line) and CM5 (dashed line) differentially expressed genes (DEGs). Color indicates significance of enrichment (Inf = infinite, N.S. = not significant) and dot size represents the percentage of subcluster DEGs contained within the term. **(F)** Barchart of the percent of total emerging DEGs (eDEGs, identified in bulk RNA-seq) that overlap with disease-specific DEGs at each timepoint (*Lmna*-cKO versus *Lmna*-cWT, left of the dotted line) or subcluster-specific DEGs (right of the dotted line). Barplot color indicates whether the eDEG and corresponding DEG are in the same (both up- or down-regulated; light gray) or opposite (one up- and one down-regulated; dark gray) fold change direction. The total number of DEGs is indicated below each condition. **(G)** High confidence protein-protein interaction (PPI) network generated using eDEGs overlapping subcluster CM3-specific DEGs. Color indicates log 2-fold change (Log2FC), node protein names are highlighted, and line thickness represents the degree of confidence (≥ 0.7).

Cardiomyocyte subclusters CM3 and CM5 show activation of signaling pathways related to cytosolic DNA response and extracellular matrix (ECM) communication

The identification of disease-specific cardiomyocyte subclusters that are responsible for a large fraction of the transcriptional changes observed in the hearts of *Lmna*-cKO mice suggests that cells in the CM3 and CM5 subclusters play an important role in DCM pathogenesis. To follow up on our earlier findings that many eDEGs are related to the cytosolic DNA response (Figure 3A), we investigated components of the STING pathway in more detail. Recent studies reported that cGAS, one of the major cytoplasmic DNA sensors and STING activators, is essentially absent in cardiomyocytes[28, 75, 77]. In our snRNA-seq data, very few cardiomyocytes had detectable expression of cGAS, and none of the cells in the CM3 and CM5 subclusters (Suppl. Figure S3B). Nonetheless, IPA of DEGs from subclusters CM3 and CM5 predicted several components of the STING pathway to be activated in cardiomyocytes, including Toll-like receptor-4 (TLR4), p53 (TP53), Interleukin-6 (IL6), NF-κB (NFkB), Interleukin-1 (IL1A/B), MyD88, and interferon-γ (IFNG)(Suppl. Figure S3C), and predicted activation of the GO term “cytosolic pattern recognition receptor signaling pathway” (Figure 4E). Further analysis of the snRNA-seq data revealed that several cardiomyocytes, particularly in the CM3 subclusters, expressed interferon gamma inducible protein 16 (IFI16, also known as IFI204)(Suppl. Figure S3D), another cytoplasmic DNA sensor and direct activator of STING[78]. This activation of IFI16 was specific to *Lmna*-cKO cardiomyocytes and increased with time (Suppl. Figure S3E), further supporting our hypothesis of the increased presence of cytosolic DNA in *Lmna*-cKO cardiomyocytes. The findings suggest that, despite the

absence of cGAS, cardiomyocytes can activate a cytoplasmic DNA response via IFI16 and potentially other cytoplasmic DNA sensors such as RNA polymerase III[79] or DDX41[80], which could then trigger the activation of innate immunity and other signaling pathways.

To understand whether a unique set of eDEGs in subcluster CM3 form a network of interacting proteins that together promote the observed pathogenic transcriptional changes, we built a protein-protein interaction (PPI) network using DEGs from subcluster CM3 that overlapped eDEGs filtered to retain only high confidence interactions (Figure 4G). The generated PPI network consisted of a group of upregulated genes, involved in apoptosis and proteolysis, and downregulated genes involved in cardiac function (Figure S4A). The PPI network identified CD44, a proteoglycan surface protein involved in ECM adhesion[81] (Figure 4G) as the central node through which upregulated and downregulated genes can regulate one another and drive disease progression. A high confidence PPI network built using subcluster CM5 DEGs that overlapped the eDEGs (Suppl. Figure S4B) also consisted of genes associated with the downregulation of cardiac function and the upregulation of proteolysis. This PPI network, however, was disconnected and lacked genes associated with apoptosis. These results suggest that CD44, which is only dysregulated in subcluster CM3, may play an important role in regulating pathogenic cellular processes, making it a potential target for therapeutic intervention. Subcluster CM4, despite being found in 25-dpi *Lmna*-cWT hearts, had similar representation in *Lmna*-cKO hearts (Figure 4C-D) and DEG overlap with eDEGs as subclusters CM3 and CM5 (Figure 4F). This observation may be due to a limitation of unbiased clustering to efficiently segregate nuclei from CM4 to the surrounding CM3 and CM5 subclusters. This idea is further supported by our observation that several of the eDEGs identified in CM4 are driven by nuclei in areas bordering CM3 and CM5 subclusters (Suppl. Figure S4C). Overall, these results suggest that subclusters CM3 and CM5 largely account for the transcriptional contribution of eDEGs in cardiomyocytes and are highly involved in promoting early-disease aberrant transcription.

Non-cardiomyocyte cell contribution to eDEGs takes place on a population-wide level rather than from disease-specific subclusters

Previous studies have reported changes in gene expression within non-cardiomyocyte cell populations in hearts of individuals with *LMNA*-DCM and mouse models of *Lmna*-DCM[28, 75]. Similarly, our snRNA-seq analysis identified several subclusters in non-cardiomyocyte cells that showed distinct changes in the *Lmna*-cKO hearts compared to *Lmna*-cWT controls at matching timepoints, particularly in fibroblasts and immune cells (Figure 5A-D), despite *Lmna* deletion in the *Lmna*-cKO model being restricted to cardiomyocytes. In fibroblasts, subcluster Fib3 showed decreased representation over time in *Lmna*-cKO hearts, while increasing in *Lmna*-cWT controls (Figure 5A-B). DEGs unique to subcluster Fib3 were enriched for GO terms associated with protein catabolic processes and DNA repair when compared to the other fibroblast subclusters (Figure S5A), hinting at specific functional changes in these cells. Despite the presence of *Lmna*-cKO–specific subclusters, none of the DEGs unique to individual subclusters strongly overlapped with the eDEGs identified in the bulk RNA-seq analysis (Figure 5E). In

contrast, the DEGs associated with the 25-dpi total fibroblast cluster strongly overlapped with the eDEGs (Figure 5F), suggesting that fibroblasts as a population, and not at the individual subpopulation level, substantially contribute to disease-driving aberrant gene expression, specifically in the later disease stage.

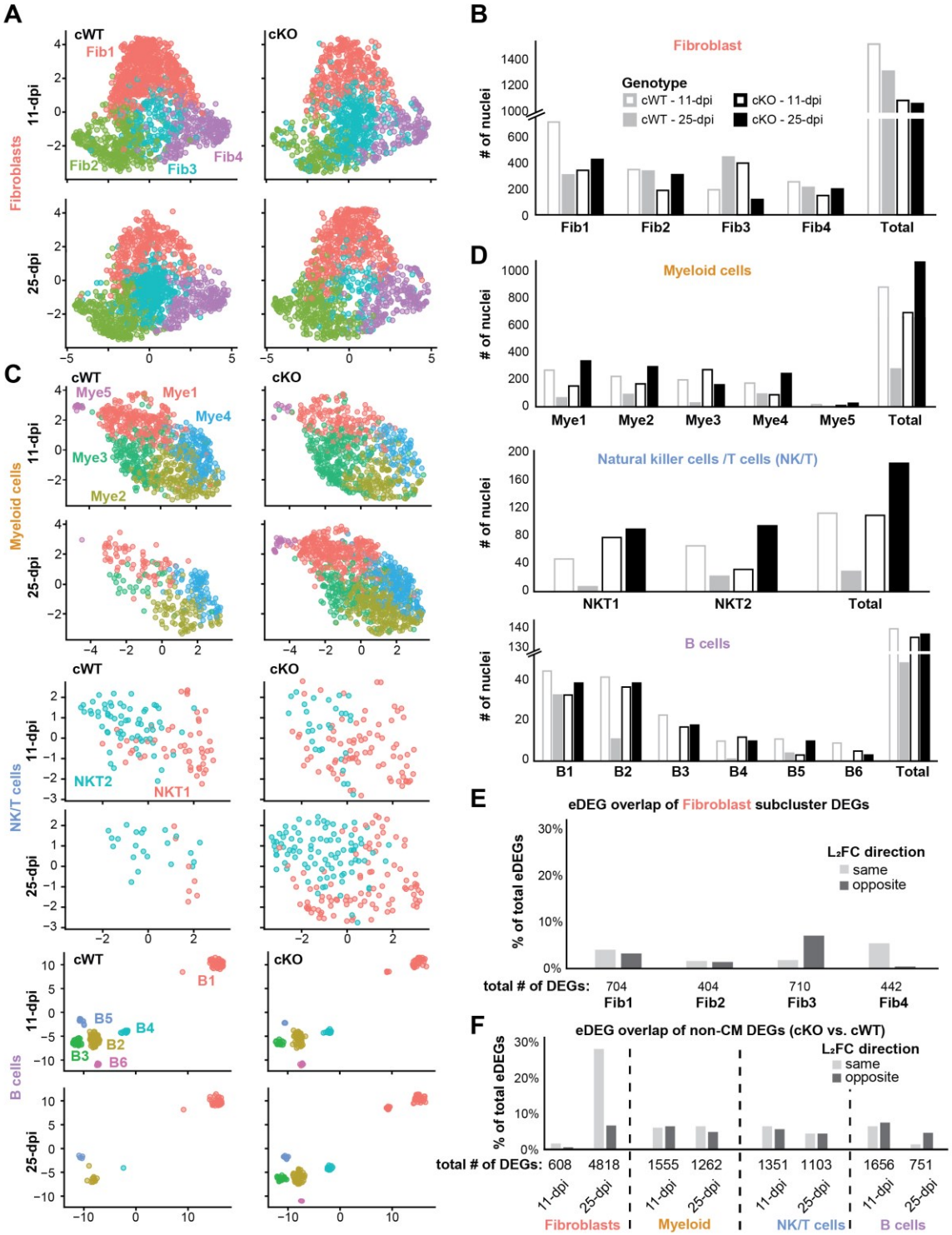

Figure 5: Non-cardiomyocyte cells contributed to aberrant expression of early disease-driving genes as a population, and not through specific subclusters. (A) UMAP plots of fibroblast-annotated nuclei from integrated snRNA-seq data, across genotype (left and right) and time point (top and bottom). Individual colors represent unique subclusters identified (Fib1-4). **(B)** Barchart of the number of nuclei captured in each genotype within individual Fib subcluster and in total. **(C)** UMAP plots of immune cell-annotated nuclei from integrated snRNA-seq data, across genotype (left and right) and time point (top and bottom). Individual colors represent unique subclusters identified (Myeloid: Mye1-5, NK/T cell: NKT1-2, and B cell: B1-6). **(D)** Barchart of the number of nuclei captured in each genotype within individual immune cell subclusters and in total. Barchart of the percent of total emerging differentially expressed genes (eDEGs) (identified in bulk RNA-seq) that overlap with **(E)** Fib subcluster-specific DEGs or **(F)** disease-specific DEGs (*Lmna*-cKO versus *Lmna*-cWT) at each timepoint for individual cell types (separated by dotted line). Barplot color indicates whether the eDEG and corresponding DEG are in the same (both up- or down-regulated; light gray) or opposite (one up- and one down-regulated; dark gray) fold change direction. The total number of DEGs is indicated below each condition.

In contrast to fibroblasts, for which we did not detect an increased presence in *Lmna*-cKO hearts (Fig. 5B), our snRNA-seq analysis revealed an increase of immune cells in the *Lmna*-cKO hearts compared to the very low levels seen in the hearts of *Lmna*-cWT controls (Figure 5C-D). These findings are consistent with previous *LMNA*-DCM studies[28, 75] and reports that cardiomyocytes, in response to injury, release cytokines and recruit immune cells, leading to inflammation and further induction of cardiac remodeling[82, 83]. Due to the low numbers of immune cells in the *Lmna*-cWT hearts at 25-dpi, determining disease-specific immune cell subclusters was challenging. Nonetheless, our data indicate that B cell levels were generally consistent between 11- and 25-dpi *Lmna*-cKO hearts and similar to those in *Lmna*-cWT hearts, whereas myeloid and NK/T cell subclusters increased in *Lmna*-cKO hearts throughout disease progression (Figure 5C-D). The specific increase in innate immune cells, compared to adaptive immune cells, agrees with our RNA-seq data, in which eDEGs and 25-dpi DEGs were specifically enriched for GO terms related to innate immunity (Figure 3A). Overall, across all immune cells, we observed limited but consistent overlap between *Lmna*-cKO specific DEGs and eDEGs (Figure 5F), with no individual subcluster showing a particularly pronounced overlap with eDEG (Figure S5B), resembling what was observed in fibroblasts (Figure 5E). Taken together, these data indicate that non-cardiomyocytes, specifically fibroblasts and innate immune cells, substantially contribute to the transcriptomic changes identified in the bulk-RNA-seq analysis, particularly at 25-dpi.

Deconvolution validates the distribution of eDEGs among distinct cell types

Bulk RNA-seq and snRNA-seq both provide unique perspectives of the transcriptome, enabling us to identify early disease-driving genes and the differential expression of individual cell types, respectively. To combine the respective strengths of each method, we performed deconvolution with BayesPrism[43] (Figure 6A). Deconvolution uses the cell type-specific annotations of the transcriptome determined by snRNA-seq to infer the

contribution of each cell type in the high-resolution data generated by bulk RNA-seq. This technique allowed us to further validate our observations related to eDEGs within individual cell types. It is important to note, however, that deconvolution cannot parse out the contribution of individual cell type subpopulations (Figures 4C, 5A, and 5C), as their genome-wide transcriptomes are too similar, despite the obvious differences detected in the snRNA-seq data.

We first inferred the cell type composition of each bulk RNA-seq sample using the deconvolution algorithm and our snRNA-seq data (Figure 6B). Unbiased hierarchical clustering of the deconvolved cell composition segregated samples efficiently by genotype and timepoint (Figure 6B), with some minor overlap for the early timepoint, mirroring the bulk RNA-seq PCA results (Figure 2B). Clustering of the deconvolved cell composition appeared to be driven by the increased transcriptional representation of innate immune cells (i.e., NK/T and myeloid cells) in *Lmna*-cKO samples over time, at the expense of other cell types, such as endothelial cells. Adaptive immune cells (i.e., B cells) on the other hand, appeared much less pronounced in *Lmna*-cKO hearts compared to *Lmna*-cWT samples. These findings further corroborate our immunofluorescence (Figures 3E-F) and snRNA-seq (Figure 5D) data that innate, but not adaptive, immunity drives immune response in *Lmna*-cKO hearts. Fibroblast transcriptional representation remained unchanged over time in *Lmna*-cKO hearts, whereas it decreased in *Lmna*-cWT hearts at 25-dpi (Figure 6B). These results suggest that although fibroblast numbers remain nearly constant over time in both *Lmna*-cKO and *Lmna*-cWT hearts (Figure 5B), their transcriptional output decreases with time in the healthy *Lmna*-cWT hearts, but not in the *Lmna*-cKO hearts, where the fibroblasts instead exhibit distinct changes in the genes expressed (Figure 5A, F).

Next, we aimed to understand the contribution of specific cell types to the eDEGs we had identified in our bulk RNA-seq analysis (Figure 2C-E). To achieve this, we deconvolved the bulk RNA-seq count matrix and identified DEGs between *Lmna*-cKO and *Lmna*-cWT gene expression at 11-dpi in each cell type (p-adj < 0.05; but without a |log2-FC| threshold). These 'deconvolved DEGs' were checked for overlap with the eDEGs and used for further analysis. Cardiomyocyte and fibroblasts had by far the largest number of 11-dpi deconvolved DEGs that overlapped with eDEGs (Figure 6C; Suppl. Figure S6A), as expected based on their substantial transcriptional contribution (Figure 6B). Both cardiomyocytes and fibroblasts showed strong activation of interferon signaling and autophagy pathways (Suppl. Figure S6B), suggesting that these cell types are primarily responsible for the detection of these pathways in bulk RNA-seq data. Overall, more than 85% of eDEGs (corresponding to 426 genes) overlapped with the deconvolved DEGs for cardiomyocytes, fibroblasts, NK/T cells, and Myeloid cells (Figure 6C). Of these 426 eDEGs, 229 were unique to deconvolved DEGs assigned to cardiomyocytes, highlighting the substantial role of cardiomyocytes in driving the eDEG response. These data are in good agreement with our snRNA-seq data, which also identified a substantial overlap between the cardiomyocyte cluster transcriptomic changes and the eDEGs (Figure 4F). Of the 496 total eDEGs, 70 eDEGs (≈14.1%) did not overlap with 11-dpi deconvolved DEGs from either of the cell types of interest (Figure 6C), suggesting that a fraction of

eDEGs may arise from changes in a combination of cell types, and/or from difficulties of the deconvolution algorithm to assign transcriptomic data to specific cell types.

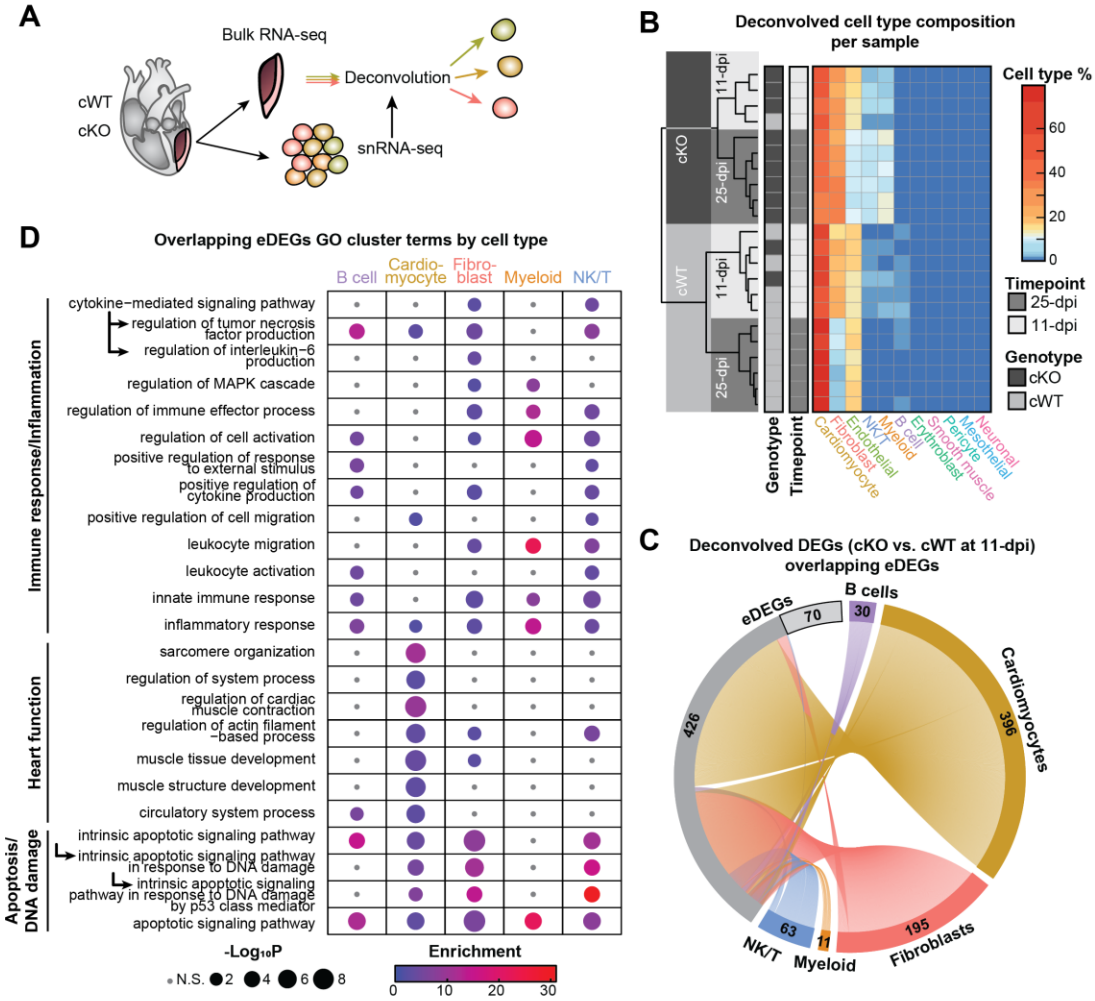

Figure 6: Bulk RNA-seq deconvolution identifies the transcriptional contribution of individual cell types in *Lmna*-cKO hearts. (A) Schematic depicting the use of single nucleus RNA sequencing (snRNA-seq) to infer cell type-specific transcriptional contribution from the deconvolved bulk RNA-seq data of *Lmna*-cKO (cKO) and *Lmna*-cWT (cWT) samples. **(B)** Heatmap of deconvolved transcriptional cell type composition for each sample. Columns indicate unique cell types and rows indicate individual samples. Rows are sorted using unbiased hierarchical clustering, with experimental conditions denoted on the left side by color. **(C)** Circos plot connecting individual emerging differentially expressed genes (eDEGs), identified in bulk RNA-seq, to deconvolved DEGs (*Lmna*-cKO vs. *Lmna*-cWT) at 11-dpi for different cell types. The number of genes represented, and the corresponding cell type are indicated. **(D)** Dot plot matrix of Gene Ontology (GO) cluster terms enriched in eDEGs overlapping deconvolved DEGs at 11-dpi for each individual cell type (columns). Arrows indicate child terms present below their respective parent term. Dot size represents significance of the term enrichment (N.S. = not significant) and dot color indicates term enrichment.

To understand which cell types primarily contribute to the functional processes associated with the eDEGs (Figure 3A), we performed a GO term analysis of the deconvolved DEGs and overlapping eDEGs (Figure 6D). We found a clear enrichment of cell-type specific GO terms associated with each cell population, confirming deconvolution's ability to reliability assign gene contribution to the appropriate cell type. For example, GO terms linked to heart function were assigned to the cardiomyocyte population, whereas immune response/inflammation GO terms were largely represented in immune cells, along with fibroblasts (Figure 6D). The involvement of fibroblasts in this GO term category suggests that fibroblasts play an important role in supporting immune response activation and inflammation in *Lmna*-cKO hearts. GO terms related to DNA damage and apoptosis were enriched in eDEGs associated with cardiomyocytes, fibroblasts, and NK/T cells (Figure 6D). Together, these results further support the idea that cardiomyocytes in *Lmna*-cKO hearts experience DNA damage (Figure 3B-D) and nuclear envelope damage [28, 73], which triggers DNA damage responses, cytosolic DNA responses, and other signaling pathways that promote cardiomyocyte dysfunction, signal to non-cardiomyocytes, and ultimately contribute to aberrant heart function.

Cell-cell communication analysis reveals altered ECM-receptor signaling during disease progression in *Lmna*-cKO hearts

The snRNA-seq and deconvolution analyses suggest the involvement of multiple cell types contributing to the identified eDEGs and the cardiac disease pathogenesis in *Lmna*-cKO mice. Furthermore, the enrichment of DEGs in the cardiomyocyte subclusters CM3/CM5 for GO terms involved in cell adhesion and communication (Figure 4E, S3A), and the IPA upstream regulator predictions (Table 1) indicate that intercellular interactions may play a role in the disease development[84]. To infer information about altered cell-cell and cell-extracellular matrix (ECM) communication in *Lmna*-cKO hearts, we applied the CellChat[46] algorithm to our snRNA-seq transcriptomic data. We then compared cell-cell communication between *Lmna*-cKO and *Lmna*-cWT hearts at each timepoint. This analysis revealed several differences in intercellular interactions (Figure 7A). Overall, cell-cell communication was downregulated in *Lmna*-cKO versus *Lmna*-cWT hearts at 11-dpi but increased by 25-dpi (Figure 7A). Fibroblasts had a particularly strong shift from down- to up-regulated interaction strength between the 11- and 25-dpi timepoints, driving most of the outgoing signaling to innate immune cells (myeloid and NK/T cells) during the late disease timepoint, corresponding with our deconvolution findings. Myeloid and NK/T cell interactions were also upregulated at 25-dpi, further corroborating the involvement of innate immunity as opposed to adaptive immunity in disease progression. This trend, however, did not hold true for B cell, which had decreased incoming communication from all other cell types, both at 11- and 25-dpi.

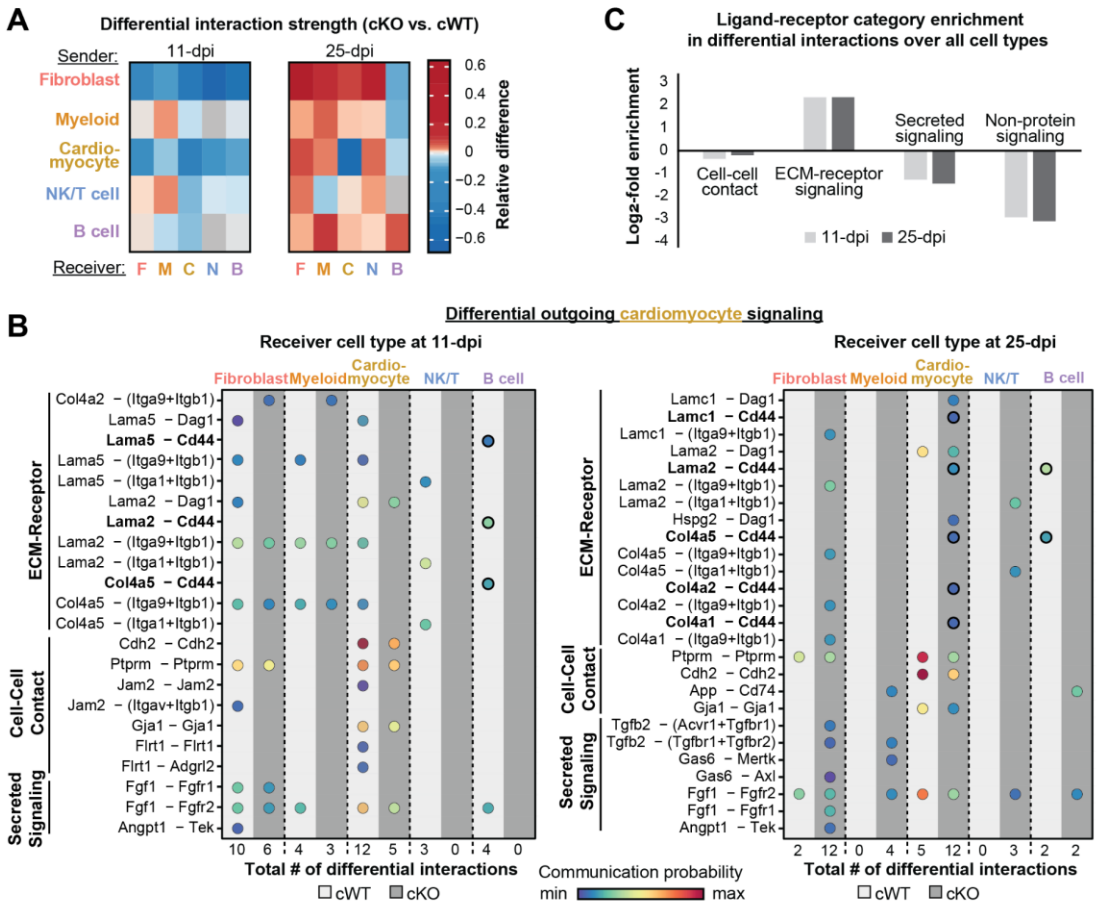

Figure 7: ECM-receptor-based cell-cell communication is highly modulated in *Lmna*-cKO hearts. (A) Heatmap showing relative difference (*Lmna*-cKO (cKO) vs. *Lmna*-cWT (cWT)) in the interaction strength of sender cell types (rows) and receiving cell types (columns, initial letter) at 11- (left) and 25-dpi (right). **(B)** Dotplot showing the degree of communication probability for individual ligand-receptor interactions (rows) between cardiomyocyte (CM, sender) and receiving cell types found to be significantly different between *Lmna*-cKO (dark gray columns) and *Lmna*-cWT (white columns) experimental conditions at both 11-dpi (left) and 25-dpi (right) timepoints. Ligand-receptor pairs are categorized based on interaction types listed in the CellChat database. The sum of differential interactions is listed below each column. Interactions mediated through Cd44 are bolded. **(C)** Barplot showing the log2 fold enrichment of particular ligand-receptor (L-R) categories associated with differential interactions over all cell types by time point (light gray - 11-dpi, dark gray - 25-dpi).

Whereas cell-cell communication overall increased in *Lmna*-cKO hearts at the 25-dpi timepoint, cardiomyocyte-to-cardiomyocyte communication strength was highly downregulated in *Lmna*-cKO versus *Lmna*-cWT hearts at both timepoints (Figure 7A). This decreased cardiomyocyte-to-cardiomyocyte interaction strength could largely be explained by the reduced number and strength of ligand-receptor signaling interactions for *Lmna*-cKO cardiomyocytes compared to *Lmna*-cWT controls at 11-dpi (Figure 7B, cardiomyocyte column). We also observed the formation of several new cardiomyocyte-

cardiomyocyte interactions at 25-dpi, albeit with low communication probability (Figure 7B). Taken together, these observations indicate that cardiomyocyte self-communication is abrogated and altered in *Lmna*-cKO hearts. Furthermore, a large portion of the new ligand-receptor interactions of *Lmna*-cKO cardiomyocytes formed for self-communication at 25-dpi involved Cd44 (71%), whereas cardiomyocyte-to-B cell communication normally taking place in *Lmna*-cWT hearts was reduced in *Lmna*-cKO hearts (Figure 7B, bold). Moreover, we observed a similar shift of Cd44-mediated cell-cell communication in fibroblasts, whose interaction shifted from B cells in *Lmna*-cWT hearts to cardiomyocytes in *Lmna*-cKO hearts at 25-dpi (Figure S7A). These findings suggest that CD44, the ECM-interacting surface glycoprotein identified as upregulated and a central node of the CM3 DEGs PPI interaction network (Figure 5E), plays an important role in the altered communication between cardiomyocytes and B cell in *Lmna*-cKO hearts. In addition to Cd44, fibroblast communication at 25-dpi with immune cells and cardiomyocytes seemed to be largely driven through Cd36 and Cd47 receptors, especially with thrombospondins (Thbs1/2/4, also known as TSP1/2/4) ECM proteins (Suppl. Figure S7A). Previous studies have noted the activation of macrophages in response to TSP1 binding to their surface CD36 receptors, resulting in increased TLR4 expression and NF-κB and TNF-α activity[85], all of which were predicted to be activated in our eDEG dataset (Table 1). This suggests that *Lmna*-cKO fibroblasts initiate immune cell activation through these ECM-receptor interactions at 25-dpi. In general, our data indicate that cardiomyocyte and non-cardiomyocyte differential interactions were largely mediated by ECM-receptor pathways (Figure 7C), in agreement with recent work in a similar *LMNA*-DCM mouse model showing that cardiomyocytes activate fibroblasts via ECM-mediated signaling[28]. Overall, our CellChat analysis indicates that cell-cell-communication, mediated by altered ECM composition and remodeling is significantly perturbed in *Lmna*-cKO hearts. This deficient communication, which is also consistent with the downregulation of genes associated with GO term such as “cell communication involved in cardiac conduction” identified in *Lmna*-cKO specific cardiomyocyte subclusters (Figure 4E), might explain the cardiac arrhythmias that are a hallmark feature in *LMNA*-DCM and contribute to the sudden cardiac death in the *Lmna*-cKO mice.

Discussion

Studies of *LMNA*-DCM in human cardiac tissue and preclinical animal models have largely been devoid of temporal analyses, with severe cardiac dysfunction and overall reduced health characteristic of late-stage disease confounding the interpretation. In the present study, we applied a multi-level transcriptomic study to an inducible *LMNA*-DCM model and compared early and late timepoints to detect early transcriptomic perturbations that might drive aberrant signaling and disease progression. At the early timepoint (11-dpi, i.e., the end of the tamoxifen washout period), cardiomyocytes in the *Lmna*-cKO model already had significantly reduced lamin A/C levels (Figure 1B-D) and hearts exhibited structural abnormalities (Figure 1G-I) and impaired function (Figure 1J-K), but transcriptomic analyses revealed substantially fewer DEGs compared to the late disease timepoint (25-dpi, Figure 2C-D). These temporal differences in cardiac function and gene expression, along with those seen in immune cell recruitment (Figure 3E-F) and cell-cell

communication (Figure 7), demonstrate the importance of investigating early transcriptional changes, represented by the eDEGs identified here.

The inducible, cardiomyocyte-specific *Lmna* deletion *Lmna*-cKO mouse model offers several advantages when trying to establish disease drivers. First, unlike complete lamin A/C deletion, the reduction in lamin A/C protein levels mimics the reduced lamin levels frequently seen in clinical cases of *LMNA*-DCM[14, 29, 58, 59]. Furthermore, the *Lmna*-cKO model closely recapitulates *LMNA*-DCM disease pathology, including ventricular wall thinning, impaired contractile function, and sudden cardiac death, although a definitive determination of the cause of death is difficult due to the lack of reliable ways to study arrhythmias in mice[86-88]. In addition, inducing lamin A/C depletion in adulthood allows for separating the effects of lamins on cardiac development from those on cardiac function. It also reduces confounding effects present in many commonly used *LMNA*-DCM animal models, such as large variability in disease onset and severity between animals, involvement of various tissues, and differences in animal size and motility between genotypes [63, 89-92]. Lastly, by combining the *Lmna*-cKO model with advanced transcriptomic analysis approaches, we were able to identify the extent and timing of the contribution of specific cell types to cardiac dysfunction in the *Lmna*-cKO mice, including a subset of cardiomyocytes that drive many of the transcriptomic changes, fibroblasts, the innate immune system, and altered cell-cell-communication.

The rapid development of severe DCM following lamin A/C depletion in cardiomyocytes is consistent with findings from recent studies using similar mouse models[22, 28, 93-95]. These models also found increased fibrosis, impaired cardiac function, and death within 3 to 5 weeks upon induction of lamin A/C depletion. All but one of those studies also reported increased DNA damage in cardiomyocytes, consistent with our immunofluorescence analysis (Figure 3B-D). In several of these studies, lamin A/C depletion led to increased apoptosis of cardiomyocytes[22, 93, 95], as predicted by our transcriptomic analysis (Figures 3A, 4E, 6D). Additionally, numerous clinical, preclinical, and cell culture models of striated muscle laminopathies have shown the presence of increased DNA damage and impaired DNA damage repair mechanisms[19-22, 25, 62, 96]. Recent findings suggest that the DNA damage and DNA damage response activation is caused by mechanical damage to fragile laminopathic nuclei in muscle cells[25, 62, 73, 97], although it is also possible that loss of lamin A/C per se contributes to altered signaling by disturbing chromatin organization and interaction with transcriptional regulators[17, 19, 20, 98].

It remains unclear, however, whether DNA damage directly promotes disease pathology, or is merely a reflection of late-stage damage to cardiomyocytes and progressive cardiomyocyte loss[14, 62, 99]. In our bulk transcriptomic analysis, normalized read counts for the *Lmna* gene were consistent in *Lmna*-cWT controls across both timepoints, whereas *Lmna* levels showed a small but significant *increase* in *Lmna*-cKO samples between the 11- and 25-dpi timepoints (Figure S2B). To test whether this increase in the *Lmna*-cKO hearts was due to either the loss of cardiomyocyte with low *Lmna* levels or the increased presence of infiltrating immune cells with high lamin A/C levels[100, 101], we quantified the percentage of Pcm1-positive nuclei amongst all detected nuclei in left ventricular tissue

at 11- and 25-dpi. The fraction of Pcm1-positive nuclei did not decrease between the different timepoints (Figure S2C), suggesting that the increased *Lmna* expression in bulk tissue results from the infiltration of innate immune cells in the *Lmna*-cKO ventricular tissue by 25-dpi (Figure 3E-F, 5C-D, 6B), and not large-scale loss of cardiomyocytes.

Our transcriptomic analysis detected the activation of signaling pathways in response to DNA damage (Figures 3A, 4E & 6D) already at the earliest timepoint, consistent with the significant subset of cardiomyocytes with DNA damage early in disease (Figure 3D-E). Nuclear envelope rupture and DNA damage could drive disease pathogenesis through multiple mechanisms beyond loss of cardiomyocytes. A recent study demonstrated that inhibiting DNA damage repair in striated muscle leads to chronic activation of p53 and increased oxidative stress, driving cardiac myocyte apoptosis, dilated cardiomyopathy, and sudden death[102]. Furthermore, nuclear envelope rupture results in exposure of genomic DNA to the cytoplasm, which could trigger STING-dependent and independent pattern recognition pathways. Although our current study did not directly measure rates of nuclear envelope rupture in cardiomyocytes, our snRNA-seq analysis identified a unique subpopulation of cardiomyocytes (i.e., subclusters CM3 and CM5) that drives much of the transcriptional changes despite representing only ~11% of all captured cardiomyocytes (CM3: 5.72%; CM5: 5.3%). This fraction of cardiomyocytes is similar in magnitude to the fraction of cardiomyocytes with DNA damage observed in our and other studies, and to the fraction of cardiomyocytes that exhibit nuclear envelope rupture in a *Lmna*-cKO model recently published by the Ikegami group[28]. Thus, it is intriguing to speculate that these subclusters represent cardiomyocytes with damaged nuclei. However, the transient nature of nuclear envelope rupture, nuclear envelope repair, and DNA damage[72, 96, 103] makes this challenging to confirm directly. Collectively, these findings support a role for DNA damage and nuclear damage as an early catalyst of disease pathology. Furthermore, the numerous pathways by which DNA damage and nuclear damage can lead to cardiac dysfunction may also explain why targeting specific pathways, such as p53 signaling, has provided only limited success in preclinical *LMNA*-DCM models [19, 22, 25], whereas reducing mechanical stress on the cardiomyocyte nuclei by disrupting the Linker of Nucleoskeleton to Cytoskeleton (LINC) complex results in near-complete rescue in mouse models with cardiomyocyte specific lamin A/C depletion[93, 94, 97].

Nuclear damage and altered signaling in lamin A/C depleted cardiomyocyte may also affect other cell types. Notably, we observed increased activation of the ERK/MAPK, autophagy, and other pathways in both cardiomyocytes and fibroblasts (Figures 6D, Suppl. Figure S6B), even though fibroblasts express normal lamin A/C levels. These findings suggest that some of these commonly reported effects may represent general stress responses and are not specific to lamin A/C depletion. On the other hand, our study revealed a clear activation of innate immunity in the *Lmna*-cKO hearts, both through immunostaining (Figures 3E-F) and transcriptomic analysis (Figures 3A, 5D, 5F, and 6B). This activation of innate immunity has been proposed to be driven by the cGAS/STING pathway[22]. We hypothesize that the activation of innate immunity following DNA damage and nuclear envelope rupture could instead be mediated by other components of the cytoplasmic pattern recognition pathway[104, 105], which we found to be specifically

upregulated in eDEGs (Figure 3A) and enriched in the disease-specific subcluster CM3 (Figures 4E & 8). Recent studies demonstrating extremely low expression of cGAS in cardiomyocytes[28], and the only limited rescue of survival in a *LMNA*-DCM mouse models with systemic cGAS deletion[22] further support this hypothesis. At the same time, it is possible that DNA released by damaged cardiomyocytes and subsequent uptake by other cells activate cytosolic patterns recognition responses in other cell types, such as macrophages and fibroblasts. These effects, possibly complemented by cytokine releases downstream of cytoplasmic pattern recognition pathways, could then additionally contribute to pathogenic processes in fibroblasts and immune cells.

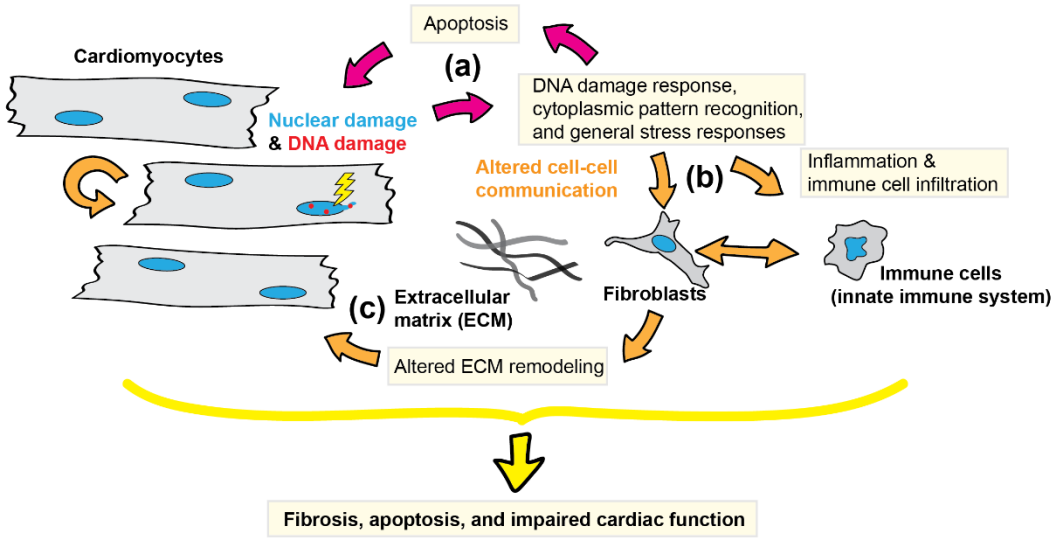

Figure 8: Proposed model for molecular mechanisms driving altered gene expression and *LMNA*-DCM pathogenesis. (a) Nuclear damage in a subset of *LMNA* laminopathic cardiomyocytes, with potentially additional contributions from altered chromatin organization and signaling in these cells, leads to DNA damage and exposure of genomic DNA to the cytoplasm. These events result in activation of cGAS-independent cytosolic pattern recognition pathways and DNA damage response pathways. **(b)** These signaling pathways trigger transcriptomic changes in cardiac fibroblasts and the recruitment of immune cells. **(c)** Altered extracellular matrix (ECM) remodeling by the fibroblasts perturbs cell-cell communication, including cardiomyocyte/cardiomyocyte and cardiomyocyte/non-cardiomyocyte communication. Activation of pattern recognition pathways in immune cells and fibroblasts triggered by DNA and other signals from damaged and apoptotic cardiomyocytes, along with additional signaling mediated by fibroblast, might further drive the response of non-cardiomyocytes. Collectively, these changes in cell-cell communication, ECM remodeling, and cardiomyocyte damage result in impaired cardiac function and development of DCM.

Furthermore, we hypothesize that cardiac ECM remodeling drives the perturbed cellular communication we detected across various cell types (Figure 7A, B). Our CellChat analysis identified ECM-based signaling as a major component of downregulated cell-cell communication throughout disease (Figure 7B). Whereas cell-cell communication subsequently increased for immune cells, fibroblasts, and cardiomyocytes at the late

disease timepoint (Figure 7B), cardiomyocyte-cardiomyocyte intercellular communication was persistently downregulated (Figures 4E & 7B). These findings, which are consistent with a recent report of altered fibroblast function in a cardiomyocyte-specific lamin A/C depletion model[28] and the transcriptional changes and early presence of fibrosis in our model, suggest that fibrosis is not only a downstream consequence of cardiac dysfunction in *LMNA*-DCM, but directly contributes to the disease pathogenesis.

Limitations of the current study. Although the *Lmna*-cKO model provides many advantages to study temporal *LMNA*-DCM disease drivers, it is important to note some limitations. The genetic landscape of *LMNA*-DCM is diverse, encompassing missense mutations, frame-shift mutations, and splice-site variants spanning all axons and the first 10 introns of the *LMNA* gene[106]. Since *LMNA* mutations are congenital and nearly ubiquitously expressed, they may directly affect cardiac development and the function of non-cardiomyocyte cardiac cell populations, which is not reflected in our model. Furthermore, other tissues affected by *LMNA* mutations might contribute to *LMNA*-DCM disease progression and severity. In addition, the analysis presented here focused on eDEGs, i.e., genes that show changes in expression early in disease, which become even more pronounced with disease progression. This analysis leaves out any DEGs identified at 25-dpi that were not detected as statistically significant at the early disease timepoint (11-dpi) or that were inconsistent with the direction of change between the two timepoints. Although we assume that such genes are primarily consequences of the disease progression, rather than disease drivers, they may nonetheless contribute to the disease. Lastly, the goal of this study was to identify early transcriptional changes. We recognize that transcription levels do not always correlate with protein levels, nor does the transcriptional analysis directly capture post-translational modifications or changes in intra- and extracellular localization of proteins. Thus, although, the predictions from the transcriptional analysis match the histological and functional measurements available to date, further studies are needed to fully validate the proposed mechanisms and to explore the suitability of identified pathways as potential therapeutic targets.

In conclusion, the temporal transcriptional analyses, enabled by our inducible *LMNA*-DCM mouse model, suggests that the early prevalence of DNA damage, cytosolic pattern recognition, and ECM changes play major roles in driving *LMNA*-DCM pathology. Our data suggest a model in which nuclear damage in cardiomyocytes leads to activation of cytosolic pattern recognition pathways, independent of cGAS, which, together with other effects triggered by loss of lamin A/C, leads to substantial transcriptional and functional changes in a small subset of cardiomyocytes. Signaling from these cardiomyocytes, along with fibroblasts mediated changes in ECM remodeling, which could occur downstream of their own cytosolic pattern recognition and other sensors, leads to the recruitment of myeloid, natural killer, and T cells to induce inflammation through their own cytosolic pattern recognition signaling pathways, further driving disease progression (Figure 8). Targeting this disturbed cell-cell-communication, and/or preventing the initial nuclear damage by reducing cytoskeletal forces on the fragile lamin mutant nuclei, could thus offer new therapeutic options for *LMNA*-DCM.

Acknowledgments

The authors thank Stephen Weiss (University of Michigan) for providing the floxed *Lmna* mice. In addition, the authors thank Hannah Erm Hwei Fong for help with tamoxifen injections, Alexander Sopilniak Mints, Hind Zahr, and Julie Heffler for help with weaning and genotyping the mice, and Charles Danko (Cornell University) for the development and use of BasePrism. Bulk RNA sequencing was performed by the Biotechnology Resource Center (BRC) Genomics Facility (RRID:SCR_021727) at the Cornell Institute of Biotechnology.

Sources of Funding

This work was supported by awards from the National Institutes of Health (R01 HL082792 and R35 GM153257 to J.L), the National Science Foundation (MCB-1715606 and URoL-2022048 to J.L.), the Volkswagen Foundation (A130142 to J.L.), the American Heart Association (postdoctoral fellowships 20POST35210660 to N.Z.S. and 23POST1023021 to J.M.), the Cornell Center for Vertebrate Genomics (CVG Scholar award to J.M.), and generous gifts from the Mills family to J.L. The content of this manuscript is solely the responsibility of the authors and does not necessarily represent the official views of the National Institutes of Health. We acknowledge the Cornell Institute of Biotechnology's BRC Imaging Facility (RRID:SCR_021727).

Disclosures

No conflicts of interest to disclose.

References

1. Luk, A., E. Ahn, G.S. Soor, and J. Butany, *Dilated cardiomyopathy: a review.* J Clin Pathol, 2009. **62**(3): p. 219-25.
2. Maron, B.J., J.A. Towbin, G. Thiene, C. Antzelevitch, D. Corrado, D. Arnett, A.J. Moss, C.E. Seidman, J.B. Young, A. American Heart, H.F. Council on Clinical Cardiology, C. Transplantation, C. Quality of, R. Outcomes, G. Functional, G. Translational Biology Interdisciplinary Working, E. Council on, and Prevention, *Contemporary definitions and classification of the cardiomyopathies: an American Heart Association Scientific Statement from the Council on Clinical Cardiology, Heart Failure and Transplantation Committee; Quality of Care and Outcomes Research and Functional Genomics and Translational Biology Interdisciplinary Working Groups; and Council on Epidemiology and Prevention.* Circulation, 2006. **113**(14): p. 1807-16.
3. Mestroni, L., B. Maisch, W.J. McKenna, K. Schwartz, P. Charron, C. Rocco, F. Tesson, A. Richter, A. Wilke, and M. Komajda, *Guidelines for the study of familial dilated cardiomyopathies. Collaborative Research Group of the European Human and Capital Mobility Project on Familial Dilated Cardiomyopathy.* Eur Heart J, 1999. **20**(2): p. 93-102.
4. Hershberger, R.E. and E. Jordan, *LMNA-Related Dilated Cardiomyopathy*, in *GeneReviews((R))*, M.P. Adam, et al., Editors. 1993: Seattle (WA).
5. Taylor, M.R., P.R. Fain, G. Sinagra, M.L. Robinson, A.D. Robertson, E. Carniel, A. Di Lenarda, T.J. Bohlmeyer, D.A. Ferguson, G.L. Brodsky, M.M. Boucek, J. Lascor, A.C. Moss, W.L. Li, G.L. Stetler, F. Muntoni, M.R. Bristow, L. Mestroni, and G. Familial Dilated Cardiomyopathy Registry Research, *Natural history of dilated cardiomyopathy due to lamin A/C gene mutations.* J Am Coll Cardiol, 2003. **41**(5): p. 771-80.
6. Parks, S.B., J.D. Kushner, D. Nauman, D. Burgess, S. Ludwigsen, A. Peterson, D. Li, P. Jakobs, M. Litt, C.B. Porter, P.S. Rahko, and R.E. Hershberger, *Lamin A/C mutation analysis in a cohort of 324 unrelated patients with idiopathic or familial dilated cardiomyopathy.* Am Heart J, 2008. **156**(1): p. 161-9.
7. Fatkin, D., C. MacRae, T. Sasaki, M.R. Wolff, M. Porcu, M. Frenneaux, J. Atherton, H.J. Vidaillet, Jr., S. Spudich, U. De Girolami, J.G. Seidman, C. Seidman, F. Muntoni, G. Muehle, W. Johnson, and B. McDonough, *Missense mutations in the rod domain of the lamin A/C gene as causes of dilated cardiomyopathy and conduction-system disease.* N Engl J Med, 1999. **341**(23): p. 1715-24.
8. Wang, X., A. Zabell, W. Koh, and W.H. Tang, *Lamin A/C Cardiomyopathies: Current Understanding and Novel Treatment Strategies.* Curr Treat Options Cardiovasc Med, 2017. **19**(3): p. 21.
9. Worman, H.J., *Cell signaling abnormalities in cardiomyopathy caused by lamin A/C gene mutations.* Biochem Soc Trans, 2018. **46**(1): p. 37-42.
10. de Leeuw, R., Y. Gruenbaum, and O. Medalia, *Nuclear Lamins: Thin Filaments with Major Functions.* Trends Cell Biol, 2018. **28**(1): p. 34-45.
11. Naetar, N., S. Ferraioli, and R. Foisner, *Lamins in the nuclear interior - life outside the lamina.* J Cell Sci, 2017. **130**(13): p. 2087-2096.
12. Perez-Serra, A., R. Toro, O. Campuzano, G. Sarquella-Brugada, P. Berne, A. Iglesias, A. Mangas, J. Brugada, and R. Brugada, *A novel mutation in lamin a/c causing familial dilated cardiomyopathy associated with sudden cardiac death.* J Card Fail, 2015. **21**(3): p. 217-25.
13. van Berlo, J.H., W.G. de Voogt, A.J. van der Kooi, J.P. van Tintelen, G. Bonne, R.B. Yaou, D. Duboc, T. Rossenbacker, H. Heidbuchel, M. de Visser, H.J. Crijns, and Y.M. Pinto, *Meta-analysis of clinical characteristics of 299 carriers of LMNA gene mutations: do lamin*

A/C mutations portend a high risk of sudden death? J Mol Med (Berl), 2005. **83**(1): p. 79-83.

14. Arbustini, E., A. Pilotto, A. Repetto, M. Grasso, A. Negri, M. Diegoli, C. Campana, L. Scelsi, E. Baldini, A. Gavazzi, and L. Tavazzi, *Autosomal dominant dilated cardiomyopathy with atrioventricular block: a lamin A/C defect-related disease.* J Am Coll Cardiol, 2002. **39**(6): p. 981-90.
15. Becane, H.M., G. Bonne, S. Varnous, A. Muchir, V. Ortega, E.H. Hammouda, J.A. Urtizberea, T. Lavergne, M. Fardeau, B. Eymard, S. Weber, K. Schwartz, and D. Duboc, *High incidence of sudden death with conduction system and myocardial disease due to lamins A and C gene mutation.* Pacing Clin Electrophysiol, 2000. **23**(11 Pt 1): p. 1661-6.
16. Hasselberg, N.E., T.F. Haland, J. Saberniak, P.H. Brekke, K.E. Berge, T.P. Leren, T. Edvardsen, and K.H. Haugaa, *Lamin A/C cardiomyopathy: young onset, high penetrance, and frequent need for heart transplantation.* Eur Heart J, 2018. **39**(10): p. 853-860.
17. Veltrop, R.J.A., M.M. Kukk, K. Topouzidou, L. Didden, A. Muchir, F.G. van Steenbeek, L.J. Schurgers, and M. Harakalova, *From gene to mechanics: a comprehensive insight into the mechanobiology of LMNA mutations in cardiomyopathy.* Cell Commun Signal, 2024. **22**(1): p. 197.
18. Zhang, X., X. Shao, R. Zhang, R. Zhu, and R. Feng, *Integrated analysis reveals the alterations that LMNA interacts with euchromatin in LMNA mutation-associated dilated cardiomyopathy.* Clin Epigenetics, 2021. **13**(1): p. 3.
19. Chen, S.N., R. Lombardi, J. Karmouch, J.Y. Tsai, G. Czernuszewicz, M.R.G. Taylor, L. Mestroni, C. Coarfa, P. Gurha, and A.J. Marian, *DNA Damage Response/TP53 Pathway Is Activated and Contributes to the Pathogenesis of Dilated Cardiomyopathy Associated With LMNA (Lamin A/C) Mutations.* Circ Res, 2019. **124**(6): p. 856-873.
20. Cheedipudi, S.M., S.J. Matkovich, C. Coarfa, X. Hu, M.J. Robertson, M. Sweet, M. Taylor, L. Mestroni, J. Cleveland, J.T. Willerson, P. Gurha, and A.J. Marian, *Genomic Reorganization of Lamin-Associated Domains in Cardiac Myocytes Is Associated With Differential Gene Expression and DNA Methylation in Human Dilated Cardiomyopathy.* Circ Res, 2019. **124**(8): p. 1198-1213.
21. Cho, S., M. Vashisth, A. Abbas, S. Majkut, K. Vogel, Y. Xia, I.L. Ivanovska, J. Irianto, M. Tewari, K. Zhu, E.D. Tichy, F. Mourkioti, H.Y. Tang, R.A. Greenberg, B.L. Prosser, and D.E. Discher, *Mechanosensing by the Lamina Protects against Nuclear Rupture, DNA Damage, and Cell-Cycle Arrest.* Dev Cell, 2019. **49**(6): p. 920-935 e5.
22. Cheedipudi, S.M., S. Asghar, and A.J. Marian, *Genetic Ablation of the DNA Damage Response Pathway Attenuates Lamin-Associated Dilated Cardiomyopathy in Mice.* JACC Basic Transl Sci, 2022. **7**(12): p. 1232-1245.
23. Tominaga, Y., M. Taira, T. Watanabe, Y. Kugo, M. Hasegawa, J. Narita, H. Ishida, R. Sakaniwa, T. Ueno, and S. Miyagawa, *Cardiomyocyte deoxyribonucleic acid damage and cardiac recovery in paediatric dilated cardiomyopathy.* Eur J Cardiothorac Surg, 2023. **63**(5).
24. Dai, Z., T. Ko, K. Fujita, S. Nomura, Y. Uemura, K. Onoue, M. Hamano, M. Katoh, S. Yamada, M. Katagiri, B. Zhang, S. Hatsuse, T. Yamada, S. Inoue, M. Kubota, K. Sawami, T. Heryed, M. Ito, E. Amiya, M. Hatano, N. Takeda, H. Morita, Y. Yamanishi, Y. Saito, and I. Komuro, *Myocardial DNA Damage Predicts Heart Failure Outcome in Various Underlying Diseases.* JACC Heart Fail, 2024. **12**(4): p. 648-661.
25. Kirby, T.J., H.C. Zahr, E.H.H. Fong, and J. Lammerding, *Eliminating elevated p53 signaling fails to rescue skeletal muscle defects or extend survival in lamin A/C-deficient mice.* Cell Death Discov, 2024. **10**(1): p. 245.
26. Wu, W., Q. Jin, C. Ostlund, K. Tanji, J.Y. Shin, J. Han, C.S. Leu, J. Kushner, and H.J. Worman, *mTOR Inhibition Prolongs Survival and Has Beneficial Effects on Heart Function*

After Onset of Lamin A/C Gene Mutation Cardiomyopathy in Mice. Circ Heart Fail, 2024. **17**(4): p. e011110.
27. Zhang, H., L. Ren, and J.C. Wu, *New Insights Into the Therapy for Lamin-Associated Dilated Cardiomyopathy.* JACC Basic Transl Sci, 2022. **7**(12): p. 1246-1248.
28. En, A., H. Bogireddi, B. Thomas, A.V. Stutzman, S. Ikegami, B. LaForest, O. Almakki, P. Pytel, I.P. Moskowitz, and K. Ikegami, *Pervasive nuclear envelope ruptures precede ECM signaling and disease onset without activating cGAS-STING in Lamin-cardiomyopathy mice.* Cell Rep, 2024. **43**(6): p. 114284.
29. Narula, N., V. Favalli, P. Tarantino, M. Grasso, A. Pilotto, R. Bellazzi, A. Serio, F.I. Gambarin, P. Charron, B. Meder, Y. Pinto, P.M. Elliott, J. Mogensen, M. Bolognesi, M. Bollati, and E. Arbustini, *Quantitative expression of the mutated lamin A/C gene in patients with cardiolaminopathy.* J Am Coll Cardiol, 2012. **60**(19): p. 1916-20.
30. Kim, Y. and Y. Zheng, *Generation and characterization of a conditional deletion allele for Lmna in mice.* Biochem Biophys Res Commun, 2013. **440**(1): p. 8-13.
31. Dobin, A., C.A. Davis, F. Schlesinger, J. Drenkow, C. Zaleski, S. Jha, P. Batut, M. Chaisson, and T.R. Gingeras, *STAR: ultrafast universal RNA-seq aligner.* Bioinformatics, 2013. **29**(1): p. 15-21.
32. Liao, Y., G.K. Smyth, and W. Shi, *featureCounts: an efficient general purpose program for assigning sequence reads to genomic features.* Bioinformatics, 2014. **30**(7): p. 923-30.
33. Love, M.I., W. Huber, and S. Anders, *Moderated estimation of fold change and dispersion for RNA-seq data with DESeq2.* Genome Biol, 2014. **15**(12): p. 550.
34. Stephens, M., P. Carbonetto, C. Dai, D. Gerard, M. Lu, L. Sun, J. Willwerscheid, N. Xiao, and M. Zeng. *ashr: Methods for Adaptive Shrinkage, using Emperical Bayes*. 2023; Available from: https://cran.r-project.org/web/packages/ashr/index.html.
35. Zheng, G.X., J.M. Terry, P. Belgrader, P. Ryvkin, Z.W. Bent, R. Wilson, S.B. Ziraldo, T.D. Wheeler, G.P. McDermott, J. Zhu, M.T. Gregory, J. Shuga, L. Montesclaros, J.G. Underwood, D.A. Masquelier, S.Y. Nishimura, M. Schnall-Levin, P.W. Wyatt, C.M. Hindson, R. Bharadwaj, A. Wong, K.D. Ness, L.W. Beppu, H.J. Deeg, C. McFarland, K.R. Loeb, W.J. Valente, N.G. Ericson, E.A. Stevens, J.P. Radich, T.S. Mikkelsen, B.J. Hindson, and J.H. Bielas, *Massively parallel digital transcriptional profiling of single cells.* Nat Commun, 2017. **8**: p. 14049.
36. Alvarez, M., E. Rahmani, B. Jew, K.M. Garske, Z. Miao, J.N. Benhammou, C.J. Ye, J.R. Pisegna, K.H. Pietilainen, E. Halperin, and P. Pajukanta, *Enhancing droplet-based single-nucleus RNA-seq resolution using the semi-supervised machine learning classifier DIEM.* Sci Rep, 2020. **10**(1): p. 11019.
37. Young, M.D. and S. Behjati, *SoupX removes ambient RNA contamination from droplet-based single-cell RNA sequencing data.* Gigascience, 2020. **9**(12).
38. McGinnis, C.S., L.M. Murrow, and Z.J. Gartner, *DoubletFinder: Doublet Detection in Single-Cell RNA Sequencing Data Using Artificial Nearest Neighbors.* Cell Syst, 2019. **8**(4): p. 329-337 e4.
39. Hocker, J.D., O.B. Poirion, F. Zhu, J. Buchanan, K. Zhang, J. Chiou, T.M. Wang, Q. Zhang, X. Hou, Y.E. Li, Y. Zhang, E.N. Farah, A. Wang, A.D. McCulloch, K.J. Gaulton, B. Ren, N.C. Chi, and S. Preissl, *Cardiac cell type-specific gene regulatory programs and disease risk association.* Sci Adv, 2021. **7**(20).
40. Koenig, A.L., I. Shchukina, J. Amrute, P.S. Andhey, K. Zaitsev, L. Lai, G. Bajpai, A. Bredemeyer, G. Smith, C. Jones, E. Terrebonne, S.L. Rentschler, M.N. Artyomov, and K.J. Lavine, *Single-cell transcriptomics reveals cell-type-specific diversification in human heart failure.* Nat Cardiovasc Res, 2022. **1**(3): p. 263-280.
41. Litvinukova, M., C. Talavera-Lopez, H. Maatz, D. Reichart, C.L. Worth, E.L. Lindberg, M. Kanda, K. Polanski, M. Heinig, M. Lee, E.R. Nadelmann, K. Roberts, L. Tuck, E.S. Fasouli, D.M. DeLaughter, B. McDonough, H. Wakimoto, J.M. Gorham, S. Samari, K.T.

Mahbubani, K. Saeb-Parsy, G. Patone, J.J. Boyle, H. Zhang, H. Zhang, A. Viveiros, G.Y. Oudit, O.A. Bayraktar, J.G. Seidman, C.E. Seidman, M. Noseda, N. Hubner, and S.A. Teichmann, *Cells of the adult human heart.* Nature, 2020. **588**(7838): p. 466-472.

42. Hao, Y., S. Hao, E. Andersen-Nissen, W.M. Mauck, 3rd, S. Zheng, A. Butler, M.J. Lee, A.J. Wilk, C. Darby, M. Zager, P. Hoffman, M. Stoeckius, E. Papalexi, E.P. Mimitou, J. Jain, A. Srivastava, T. Stuart, L.M. Fleming, B. Yeung, A.J. Rogers, J.M. McElrath, C.A. Blish, R. Gottardo, P. Smibert, and R. Satija, *Integrated analysis of multimodal single-cell data.* Cell, 2021. **184**(13): p. 3573-3587 e29.
43. Chu, T., Z. Wang, D. Pe'er, and C.G. Danko, *Cell type and gene expression deconvolution with BayesPrism enables Bayesian integrative analysis across bulk and single-cell RNA sequencing in oncology.* Nat Cancer, 2022. **3**(4): p. 505-517.
44. Danko, C.G. *BayesPrism*. 2022; Available from: https://www.bayesprism.org/.
45. Jin, S., M.V. Plikus, and Q. Nie, *CellChat for systematic analysis of cell-cell communication from single-cell and spatially resolved transcriptomics.* bioRxiv, 2023: p. 2023.11.05.565674.
46. Jin, S., C.F. Guerrero-Juarez, L. Zhang, I. Chang, R. Ramos, C.H. Kuan, P. Myung, M.V. Plikus, and Q. Nie, *Inference and analysis of cell-cell communication using CellChat.* Nat Commun, 2021. **12**(1): p. 1088.
47. Subramanian, A., P. Tamayo, V.K. Mootha, S. Mukherjee, B.L. Ebert, M.A. Gillette, A. Paulovich, S.L. Pomeroy, T.R. Golub, E.S. Lander, and J.P. Mesirov, *Gene set enrichment analysis: a knowledge-based approach for interpreting genome-wide expression profiles.* Proc Natl Acad Sci U S A, 2005. **102**(43): p. 15545-50.
48. Mootha, V.K., C.M. Lindgren, K.F. Eriksson, A. Subramanian, S. Sihag, J. Lehar, P. Puigserver, E. Carlsson, M. Ridderstrale, E. Laurila, N. Houstis, M.J. Daly, N. Patterson, J.P. Mesirov, T.R. Golub, P. Tamayo, B. Spiegelman, E.S. Lander, J.N. Hirschhorn, D. Altshuler, and L.C. Groop, *PGC-1alpha-responsive genes involved in oxidative phosphorylation are coordinately downregulated in human diabetes.* Nat Genet, 2003. **34**(3): p. 267-73.
49. Zhou, Y., B. Zhou, L. Pache, M. Chang, A.H. Khodabakhshi, O. Tanaseichuk, C. Benner, and S.K. Chanda, *Metascape provides a biologist-oriented resource for the analysis of systems-level datasets.* Nat Commun, 2019. **10**(1): p. 1523.
50. Szklarczyk, D., R. Kirsch, M. Koutrouli, K. Nastou, F. Mehryary, R. Hachilif, A.L. Gable, T. Fang, N.T. Doncheva, S. Pyysalo, P. Bork, L.J. Jensen, and C. von Mering, *The STRING database in 2023: protein-protein association networks and functional enrichment analyses for any sequenced genome of interest.* Nucleic Acids Res, 2023. **51**(D1): p. D638-D646.
51. Kramer, A., J. Green, J. Pollard, Jr., and S. Tugendreich, *Causal analysis approaches in Ingenuity Pathway Analysis.* Bioinformatics, 2014. **30**(4): p. 523-30.
52. Ashburner, M., C.A. Ball, J.A. Blake, D. Botstein, H. Butler, J.M. Cherry, A.P. Davis, K. Dolinski, S.S. Dwight, J.T. Eppig, M.A. Harris, D.P. Hill, L. Issel-Tarver, A. Kasarskis, S. Lewis, J.C. Matese, J.E. Richardson, M. Ringwald, G.M. Rubin, and G. Sherlock, *Gene ontology: tool for the unification of biology. The Gene Ontology Consortium.* Nat Genet, 2000. **25**(1): p. 25-9.
53. Gene Ontology, C., S.A. Aleksander, J. Balhoff, S. Carbon, J.M. Cherry, H.J. Drabkin, D. Ebert, M. Feuermann, P. Gaudet, N.L. Harris, D.P. Hill, R. Lee, H. Mi, S. Moxon, C.J. Mungall, A. Muruganugan, T. Mushayahama, P.W. Sternberg, P.D. Thomas, K. Van Auken, J. Ramsey, D.A. Siegele, R.L. Chisholm, P. Fey, M.C. Aspromonte, M.V. Nugnes, F. Quaglia, S. Tosatto, M. Giglio, S. Nadendla, G. Antonazzo, H. Attrill, G. Dos Santos, S. Marygold, V. Strelets, C.J. Tabone, J. Thurmond, P. Zhou, S.H. Ahmed, P. Asanitthong, D. Luna Buitrago, M.N. Erdol, M.C. Gage, M. Ali Kadhum, K.Y.C. Li, M. Long, A. Michalak, A. Pesala, A. Pritazahra, S.C.C. Saverimuttu, R. Su, K.E. Thurlow, R.C. Lovering, C.

Logie, S. Oliferenko, J. Blake, K. Christie, L. Corbani, M.E. Dolan, H.J. Drabkin, D.P. Hill, L. Ni, D. Sitnikov, C. Smith, A. Cuzick, J. Seager, L. Cooper, J. Elser, P. Jaiswal, P. Gupta, P. Jaiswal, S. Naithani, M. Lera-Ramirez, K. Rutherford, V. Wood, J.L. De Pons, M.R. Dwinell, G.T. Hayman, M.L. Kaldunski, A.E. Kwitek, S.J.F. Laulederkind, M.A. Tutaj, M. Vedi, S.J. Wang, P. D'Eustachio, L. Aimo, K. Axelsen, A. Bridge, N. Hyka-Nouspikel, A. Morgat, S.A. Aleksander, J.M. Cherry, S.R. Engel, K. Karra, S.R. Miyasato, R.S. Nash, M.S. Skrzypek, S. Weng, E.D. Wong, E. Bakker, T.Z. Berardini, L. Reiser, A. Auchincloss, K. Axelsen, G. Argoud-Puy, M.C. Blatter, E. Boutet, L. Breuza, A. Bridge, C. Casals-Casas, E. Coudert, A. Estreicher, M. Livia Famiglietti, M. Feuermann, A. Gos, N. Gruaz-Gumowski, C. Hulo, N. Hyka-Nouspikel, F. Jungo, P. Le Mercier, D. Lieberherr, P. Masson, A. Morgat, I. Pedruzzi, L. Pourcel, S. Poux, C. Rivoire, S. Sundaram, A. Bateman, E. Bowler-Barnett, A.J.H. Bye, P. Denny, A. Ignatchenko, R. Ishtiaq, A. Lock, Y. Lussi, M. Magrane, M.J. Martin, S. Orchard, P. Raposo, E. Speretta, N. Tyagi, K. Warner, R. Zaru, A.D. Diehl, R. Lee, J. Chan, S. Diamantakis, D. Raciti, M. Zarowiecki, M. Fisher, C. James-Zorn, V. Ponferrada, A. Zorn, S. Ramachandran, L. Ruzicka and M. Westerfield, *The Gene Ontology knowledgebase in 2023.* Genetics, 2023. **224**(1).

54. Milacic, M., D. Beavers, P. Conley, C. Gong, M. Gillespie, J. Griss, R. Haw, B. Jassal, L. Matthews, B. May, R. Petryszak, E. Ragueneau, K. Rothfels, C. Sevilla, V. Shamovsky, R. Stephan, K. Tiwari, T. Varusai, J. Weiser, A. Wright, G. Wu, L. Stein, H. Hermjakob, and P. D'Eustachio, *The Reactome Pathway Knowledgebase 2024.* Nucleic Acids Res, 2024. **52**(D1): p. D672-D678.
55. Kassambara, A. *ggpubr: 'ggplot2' Based Publication Ready Plots. R package version 0.6.0*. 2023; Available from: https://rpkgs.datanovia.com/ggpubr/.
56. Hasper, J., K. Welle, K. Swovick, J. Hryhorenko, S. Ghaemmaghami, and A. Buchwalter, *Long lifetime and tissue-specific accumulation of lamin A/C in Hutchinson-Gilford progeria syndrome.* J Cell Biol, 2024. **223**(1).
57. Zhang, H., J.E. Kieckhaefer, and K. Cao, *Mouse models of laminopathies.* Aging Cell, 2013. **12**(1): p. 2-10.
58. Verga, L., M. Concardi, A. Pilotto, O. Bellini, M. Pasotti, A. Repetto, L. Tavazzi, and E. Arbustini, *Loss of lamin A/C expression revealed by immuno-electron microscopy in dilated cardiomyopathy with atrioventricular block caused by LMNA gene defects.* Virchows Arch, 2003. **443**(5): p. 664-71.
59. Jimenez-Alcantara, I., E. Lozano-Velasco, S. Cano-Carrillo, J.M. Castillo-Casas, A.B. Garcia-Ruano, J.M. Segura-Aumente, J.A. Urbano-Moral, and D. Franco, *LMNA p.Arg624His Variant Reduces Lamin Expression at mRNA Level: Elucidating Molecular Pathways toward Cardiac Involvement in Laminopathies.* J Cardiovasc Transl Res, 2024.
60. Muchir, A., P. Pavlidis, V. Decostre, A.J. Herron, T. Arimura, G. Bonne, and H.J. Worman, *Activation of MAPK pathways links LMNA mutations to cardiomyopathy in Emery-Dreifuss muscular dystrophy.* J Clin Invest, 2007. **117**(5): p. 1282-93.
61. Anderson, C.L., K.A. Brown, R.J. North, J.K. Walters, S.T. Kaska, M.R. Wolff, T.J. Kamp, Y. Ge, and L.L. Eckhardt, *Global Proteomic Analysis Reveals Alterations in Differentially Expressed Proteins between Cardiopathic Lamin A/C Mutations.* J Proteome Res, 2024. **23**(6): p. 1970-1982.
62. Earle, A.J., T.J. Kirby, G.R. Fedorchak, P. Isermann, J. Patel, S. Iruvanti, S.A. Moore, G. Bonne, L.L. Wallrath, and J. Lammerding, *Mutant lamins cause nuclear envelope rupture and DNA damage in skeletal muscle cells.* Nat Mater, 2020. **19**(4): p. 464-473.
63. Sullivan, T., D. Escalante-Alcalde, H. Bhatt, M. Anver, N. Bhat, K. Nagashima, C.L. Stewart, and B. Burke, *Loss of A-type lamin expression compromises nuclear envelope integrity leading to muscular dystrophy.* J Cell Biol, 1999. **147**(5): p. 913-20.
64. Vigouroux, C., M. Auclair, E. Dubosclard, M. Pouchelet, J. Capeau, J.C. Courvalin, and B. Buendia, *Nuclear envelope disorganization in fibroblasts from lipodystrophic patients with*

heterozygous R482Q/W mutations in the lamin A/C gene. J Cell Sci, 2001. **114**(Pt 24): p. 4459-68.
65. Fidzianska, A. and I. Hausmanowa-Petrusewicz, *Architectural abnormalities in muscle nuclei. Ultrastructural differences between X-linked and autosomal dominant forms of EDMD.* J Neurol Sci, 2003. **210**(1-2): p. 47-51.
66. Fidzianska, A., D. Toniolo, and I. Hausmanowa-Petrusewicz, *Ultrastructural abnormality of sarcolemmal nuclei in Emery-Dreifuss muscular dystrophy (EDMD).* J Neurol Sci, 1998. **159**(1): p. 88-93.
67. Park, Y.E., Y.K. Hayashi, K. Goto, H. Komaki, Y. Hayashi, T. Inuzuka, S. Noguchi, I. Nonaka, and I. Nishino, *Nuclear changes in skeletal muscle extend to satellite cells in autosomal dominant Emery-Dreifuss muscular dystrophy/limb-girdle muscular dystrophy 1B.* Neuromuscul Disord, 2009. **19**(1): p. 29-36.
68. Gupta, P., Z.T. Bilinska, N. Sylvius, E. Boudreau, J.P. Veinot, S. Labib, P.M. Bolongo, A. Hamza, T. Jackson, R. Ploski, M. Walski, J. Grzybowski, E. Walczak, G. Religa, A. Fidzianska, and F. Tesson, *Genetic and ultrastructural studies in dilated cardiomyopathy patients: a large deletion in the lamin A/C gene is associated with cardiomyocyte nuclear envelope disruption.* Basic Res Cardiol, 2010. **105**(3): p. 365-77.
69. Nikolova, V., C. Leimena, A.C. McMahon, J.C. Tan, S. Chandar, D. Jogia, S.H. Kesteven, J. Michalicek, R. Otway, F. Verheyen, S. Rainer, C.L. Stewart, D. Martin, M.P. Feneley, and D. Fatkin, *Defects in nuclear structure and function promote dilated cardiomyopathy in lamin A/C-deficient mice.* J Clin Invest, 2004. **113**(3): p. 357-69.
70. Uchino, R., Y.K. Nonaka, T. Horigome, S. Sugiyama, and K. Furukawa, *Loss of Drosophila A-type lamin C initially causes tendon abnormality including disintegration of cytoskeleton and nuclear lamina in muscular defects.* Dev Biol, 2013. **373**(1): p. 216-27.
71. Nader, G.P.F., S. Aguera-Gonzalez, F. Routet, M. Gratia, M. Maurin, V. Cancila, C. Cadart, A. Palamidessi, R.N. Ramos, M. San Roman, M. Gentili, A. Yamada, A. Williart, C. Lodillinsky, E. Lagoutte, C. Villard, J.L. Viovy, C. Tripodo, J. Galon, G. Scita, N. Manel, P. Chavrier, and M. Piel, *Compromised nuclear envelope integrity drives TREX1-dependent DNA damage and tumor cell invasion.* Cell, 2021. **184**(20): p. 5230-5246 e22.
72. Kalukula, Y., A.D. Stephens, J. Lammerding, and S. Gabriele, *Mechanics and functional consequences of nuclear deformations.* Nat Rev Mol Cell Biol, 2022. **23**(9): p. 583-602.
73. Pavlov, D.A., C.S. Corredera, M. Dehghany, J. Heffler, K.M. Shen, N. Zuela-Sopilniak, R. Randell, K. Uchida, R. Jain, V. Shenoy, J. Lammerding, and B. Prosser, *Microtubule forces drive nuclear damage in LMNA cardiomyopathy.* bioRxiv, 2024: p. 2024.02.10.579774.
74. Pan, J., C.J. Fei, Y. Hu, X.Y. Wu, L. Nie, and J. Chen, *Current understanding of the cGAS-STING signaling pathway: Structure, regulatory mechanisms, and related diseases.* Zool Res, 2023. **44**(1): p. 183-218.
75. Reichart, D., E.L. Lindberg, H. Maatz, A.M.A. Miranda, A. Viveiros, N. Shvetsov, A. Gartner, E.R. Nadelmann, M. Lee, K. Kanemaru, J. Ruiz-Orera, V. Strohmenger, D.M. DeLaughter, G. Patone, H. Zhang, A. Woehler, C. Lippert, Y. Kim, E. Adami, J.M. Gorham, S.N. Barnett, K. Brown, R.J. Buchan, R.A. Chowdhury, C. Constantinou, J. Cranley, L.E. Felkin, H. Fox, A. Ghauri, J. Gummert, M. Kanda, R. Li, L. Mach, B. McDonough, S. Samari, F. Shahriaran, C. Yapp, C. Stanasiuk, P.I. Theotokis, F.J. Theis, A. van den Bogaerdt, H. Wakimoto, J.S. Ware, C.L. Worth, P.J.R. Barton, Y.A. Lee, S.A. Teichmann, H. Milting, M. Noseda, G.Y. Oudit, M. Heinig, J.G. Seidman, N. Hubner, and C.E. Seidman, *Pathogenic variants damage cell composition and single cell transcription in cardiomyopathies.* Science, 2022. **377**(6606): p. eabo1984.
76. Muller, A.L. and N.S. Dhalla, *Role of various proteases in cardiac remodeling and progression of heart failure.* Heart Fail Rev, 2012. **17**(3): p. 395-409.

77. Baldarelli, R.M., C.L. Smith, M. Ringwald, J.E. Richardson, C.J. Bult, and G. Mouse Genome Informatics, *Mouse Genome Informatics: an integrated knowledgebase system for the laboratory mouse.* Genetics, 2024. **227**(1).
78. Unterholzner, L., S.E. Keating, M. Baran, K.A. Horan, S.B. Jensen, S. Sharma, C.M. Sirois, T. Jin, E. Latz, T.S. Xiao, K.A. Fitzgerald, S.R. Paludan, and A.G. Bowie, *IFI16 is an innate immune sensor for intracellular DNA.* Nat Immunol, 2010. **11**(11): p. 997-1004.
79. Kessler, A.C. and R.J. Maraia, *The nuclear and cytoplasmic activities of RNA polymerase III, and an evolving transcriptome for surveillance.* Nucleic Acids Res, 2021. **49**(21): p. 12017-12034.
80. Winstone, L., Y. Jung, and Y. Wu, *DDX41: exploring the roles of a versatile helicase.* Biochem Soc Trans, 2024. **52**(1): p. 395-405.
81. Jackson, D.G., J.I. Bell, R. Dickinson, J. Timans, J. Shields, and N. Whittle, *Proteoglycan forms of the lymphocyte homing receptor CD44 are alternatively spliced variants containing the v3 exon.* J Cell Biol, 1995. **128**(4): p. 673-85.
82. Wang, E., R. Zhou, T. Li, Y. Hua, K. Zhou, Y. Li, S. Luo, and Q. An, *The Molecular Role of Immune Cells in Dilated Cardiomyopathy.* Medicina (Kaunas), 2023. **59**(7).
83. Gerbino, A., C. Forleo, S. Milano, F. Piccapane, G. Procino, M. Pepe, M. Piccolo, P. Guida, N. Resta, S. Favale, M. Svelto, and M. Carmosino, *Pro-inflammatory cytokines as emerging molecular determinants in cardiolaminopathies.* J Cell Mol Med, 2021. **25**(23): p. 10902-10915.
84. Casarella, S., F. Ferla, D. Di Francesco, E. Canciani, M. Rizzi, and F. Boccafoschi, *Focal Adhesion's Role in Cardiomyocytes Function: From Cardiomyogenesis to Mechanotransduction.* Cells, 2024. **13**(8).
85. Li, Y., X. Qi, X. Tong, and S. Wang, *Thrombospondin 1 activates the macrophage Toll-like receptor 4 pathway.* Cell Mol Immunol, 2013. **10**(6): p. 506-12.
86. Calvet, C. and P. Seebeck, *What to consider for ECG in mice-with special emphasis on telemetry.* Mamm Genome, 2023. **34**(2): p. 166-179.
87. Navarro-Garcia, J.A., F. Bruns, O.M. Moore, M.A. Tekook, D. Dobrev, C.Y. Miyake, and X.H.T. Wehrens, *In Vivo Cardiac Electrophysiology in Mice: Determination of Atrial and Ventricular Arrhythmic Substrates.* Curr Protoc, 2024. **4**(2): p. e994.
88. Tomsits, P., K.R. Chataut, A.S. Chivukula, L. Mo, R. Xia, D. Schuttler, and S. Clauss, *Analyzing Long-Term Electrocardiography Recordings to Detect Arrhythmias in Mice.* J Vis Exp, 2021(171).
89. Mounkes, L.C., S.V. Kozlov, J.N. Rottman, and C.L. Stewart, *Expression of an LMNA-N195K variant of A-type lamins results in cardiac conduction defects and death in mice.* Hum Mol Genet, 2005. **14**(15): p. 2167-80.
90. Arimura, T., A. Helbling-Leclerc, C. Massart, S. Varnous, F. Niel, E. Lacene, Y. Fromes, M. Toussaint, A.M. Mura, D.I. Keller, H. Amthor, R. Isnard, M. Malissen, K. Schwartz, and G. Bonne, *Mouse model carrying H222P-Lmna mutation develops muscular dystrophy and dilated cardiomyopathy similar to human striated muscle laminopathies.* Hum Mol Genet, 2005. **14**(1): p. 155-69.
91. Sztretye, M., L. Szabo, N. Dobrosi, J. Fodor, P. Szentesi, J. Almassy, Z.E. Magyar, B. Dienes, and L. Csernoch, *From Mice to Humans: An Overview of the Potentials and Limitations of Current Transgenic Mouse Models of Major Muscular Dystrophies and Congenital Myopathies.* Int J Mol Sci, 2020. **21**(23).
92. Stewart, C.L., S. Kozlov, L.G. Fong, and S.G. Young, *Mouse models of the laminopathies.* Exp Cell Res, 2007. **313**(10): p. 2144-56.
93. Chai, R.J., H. Werner, P.Y. Li, Y.L. Lee, K.T. Nyein, I. Solovei, T.D.A. Luu, B. Sharma, R. Navasankari, M. Maric, L.Y.E. Sim, Y.J. Loh, E. Aliwarga, J.W.L. Cheong, A. Chojnowski, M.I. Autio, Y. Haiyang, K.K. Boon Tan, C.T. Keng, S.L. Ng, W.L. Chew, M. Ferenczi, B. Burke, R.S.Y. Foo, and C.L. Stewart, *Disrupting the LINC complex by AAV mediated gene*

transduction prevents progression of Lamin induced cardiomyopathy. Nat Commun, 2021. **12**(1): p. 4722.
94. Tan, C.Y., P.S. Chan, H. Tan, S.W. Tan, C.J.M. Lee, J.W. Wang, S. Ye, H. Werner, Y.J. Loh, Y.L. Lee, M. Ackers-Johnson, R.S.Y. Foo, and J. Jiang, *Systematic in vivo candidate evaluation uncovers therapeutic targets for LMNA dilated cardiomyopathy and risk of Lamin A toxicity.* J Transl Med, 2023. **21**(1): p. 690.
95. Auguste, G., L. Rouhi, S.J. Matkovich, C. Coarfa, M.J. Robertson, G. Czernuszewicz, P. Gurha, and A.J. Marian, *BET bromodomain inhibition attenuates cardiac phenotype in myocyte-specific lamin A/C-deficient mice.* J Clin Invest, 2020. **130**(9): p. 4740-4758.
96. Wallace, M., H. Zahr, S. Perati, C.D. Morsink, L.E. Johnson, A.M. Gacita, S. Lai, L.L. Wallrath, I.J. Benjamin, E.M. McNally, T.J. Kirby, and J. Lammerding, *Nuclear damage in LMNA mutant iPSC-derived cardiomyocytes is associated with impaired lamin localization to the nuclear envelope.* Mol Biol Cell, 2023. **34**(12): p. mbcE21100527.
97. Leong, E.L., N.T. Khaing, B. Cadot, W.L. Hong, S. Kozlov, H. Werner, E.S.M. Wong, C.L. Stewart, B. Burke, and Y.L. Lee, *Nesprin-1 LINC complexes recruit microtubule cytoskeleton proteins and drive pathology in Lmna-mutant striated muscle.* Hum Mol Genet, 2023. **32**(2): p. 177-191.
98. Buxboim, A., R. Kronenberg-Tenga, S. Salajkova, N. Avidan, H. Shahak, A. Thurston, and O. Medalia, *Scaffold, mechanics and functions of nuclear lamins.* FEBS Lett, 2023. **597**(22): p. 2791-2805.
99. Malhotra, R. and P.K. Mason, *Lamin A/C deficiency as a cause of familial dilated cardiomyopathy.* Curr Opin Cardiol, 2009. **24**(3): p. 203-8.
100. Saez, A., B. Herrero-Fernandez, R. Gomez-Bris, B. Somovilla-Crespo, C. Rius, and J.M. Gonzalez-Granado, *Lamin A/C and the Immune System: One Intermediate Filament, Many Faces.* Int J Mol Sci, 2020. **21**(17).
101. Fang, C., Z. Lv, Z. Yu, K. Wang, C. Xu, Y. Li, and Y. Wang, *Exploration of dilated cardiomyopathy for biomarkers and immune microenvironment: evidence from RNA-seq.* BMC Cardiovasc Disord, 2022. **22**(1): p. 320.
102. Henpita, C., R. Vyas, C.L. Healy, T.L. Kieu, A.U. Gurkar, M.J. Yousefzadeh, Y. Cui, A. Lu, L.A. Angelini, R.D. O'Kelly, S.J. McGowan, S. Chandrasekhar, R.R. Vanderpool, D. Hennessy-Wack, M.A. Ross, T.N. Bachman, C. McTiernan, S.P.S. Pillai, W. Ladiges, M. Lavasani, J. Huard, D. Beer-Stolz, C.M. St Croix, S.C. Watkins, P.D. Robbins, A.L. Mora, E.E. Kelley, Y. Wang, T.D. O'Connell, and L.J. Niedernhofer, *Loss of DNA repair mechanisms in cardiac myocytes induce dilated cardiomyopathy.* Aging Cell, 2023. **22**(4): p. e13782.
103. Mannino, P.J. and C.P. Lusk, *Quality control mechanisms that protect nuclear envelope identity and function.* J Cell Biol, 2022. **221**(9).
104. Thompson, M.R., J.J. Kaminski, E.A. Kurt-Jones, and K.A. Fitzgerald, *Pattern recognition receptors and the innate immune response to viral infection.* Viruses, 2011. **3**(6): p. 920-40.
105. Li, D. and M. Wu, *Pattern recognition receptors in health and diseases.* Signal Transduct Target Ther, 2021. **6**(1): p. 291.
106. Bonne, G., *The UMD-LMNA mutations database.* 2020.

Tables

Top 25 predicted upstream regulators of eDEGs at 11-dpi

Upstream Regulator	Molecule Type	Predicted State	Activation z-score	-Log10(*P*-value) of Overlap	Top 10 Differentially Expressed Target Molecules in Dataset
Ifng	Cytokine	Activated	6.466	30.74	Nmrk2, **Cd24a**, H2ac6, **Hmox1**, **Hspa1a**, **Lgals3**, Ccl7, Mlana, Mafa, Dbp
Tnf	Cytokine	Activated	6.071	15.95	**Hmox1**, **Hspa1a**, **Lgals3**, Serpina3n, **Serpinb1a**, Ccl7, Mlana, Mafa, Klf5
Il1b	Cytokine	Activated	5.073	16.02	**Cd24a**, H2bc8, **Hmox1**, **Hspa1a**, Serpina3n, Ccl7, Mafa, **Cdkn1a**, S100a3, Dbp
Interferon alpha (family)	Group	Activated	4.968	12.02	**Hmox1**, **Hspa1a**, **Lgals3**, **Serpinb1a**, **Cdkn1a**, Tnfsf18, Cxcl2, Il1rn, **Atf3**, Oas1g
Il1a	Cytokine	Activated	4.662	8.92	**Hmox1**, **Serpina3n**, **Cdkn1a**, Cxcl2, Ccl2, Il1rn, S100a10, **Atf3**, Sprr1a, Ccl4
Myd88	Other	Activated	4.634	8.41	**Hmox1**, Gdf15, Tnfrsf12a, Cxcl2, Ccl2, Cebpd, Il1rn, Nppb, Maff, Ccl17
Tlr4	Transmembrane Receptor	Activated	4.632	11.59	**Hmox1**, Ccl7, Nr4a2, Cxcl2, **Ddit3**, Ccl2, Cebpd, Nppb, **Atf3**, Ccl4
App	Other	Activated	4.375	10.26	**Hmox1**, **Hspa1a**, Crabp2, **Lgals3**, Ccl7, **Cdkn1a**, Gdf15, Nr4a2, Shisa3, Cxcl2
Sting1	Ion Channel	Activated	4.329	14.47	Cxcl2, **Ddit3**, Ifi27l2a, Oas1g, Oas3, Oas2, Fcgr4, Ccl4, Pnp, Irf7
NFKB (complex)	Complex	Activated	4.292	14.27	Slc2a5, **Cd24a**, **Hmox1**, Serpina3n, Ccl7, **Cdkn1a**, Gdf15, Cgref1, Cxcl2, Dbp
Il6	Cytokine	Activated	4.274	7.71	**Hmox1**, Serpina3n, **Cdkn1a**, Tnfrsf23, Hpx, Tnfrsf12a, Cxcl2, Ccl2, Cebpd, Il1rn
Irf7	Transcription Regulator	Activated	4.262	9.11	Ccl2, Oas1g, Oas3, Oas2, Ly6a, Ube2l6, Irf7, Ifitm3, Mx2, Phf11b
Irf3	Transcription Regulator	Activated	4.235	13.75	**Cdkn1a**, Ccl2, Ifi27l2a, Oas1g, Oas3, Oas2, Ccl4, Pnp, Ube2l6, Irf7
TP53	Transcription Regulator	Activated	4.212	15.38	Peg10, **Hmox1**, **Hspa1a**, **Lgals3**, Serpina3n, Psat1, Klf5, **Cdkn1a**, Ddit4l, Dbp
Csf2	Cytokine	Activated	4.189	8.94	**Hmox1**, **Cdkn1a**, Ccl25, Gdf15, Nr4a2, Ifrd1, Cxcl2, **Ddit3**, Ccl2, Il1rn
Agt	Growth Factor	Activated	4.102	19.62	**Hspa1b**, Gabrb3, **Hmox1**, Nptx2, **Hspa1a**, Crabp2, **Lgals3**, Serpina3n, Ccl7, Klf5
Tgfb1	Growth Factor	Activated	4.095	20.08	**Hmox1**, **Hspa1a**, **Lgals3**, Serpina3n, Psat1, **Serpinb1a**, Ccl7, **Cdkn1a**, Gsta2, Dbp
LDL (complex)	Complex	Activated	4.088	16.87	**Hmox1**, Ccl7, **Cdkn1a**, Star, Nr4a2, Cxcl2, Ccl9, **Ddit3**, Ccl2, Il1rn
ERK1/2 (family)	Group	Activated	4.056	8.21	**Cdkn1a**, Star, Gnrh1, Cxcl2, **Ddit3**, Ccl2, Ccn2, Ccl4, S100a6, Rhoc
Irgm1	Enzyme	Inhibited	-4.042	11.58	Ccl2, Ifi27l2a, Oas1g, Oas3, Oas2, Apol9a, Irf7, Ifitm3, Mx2, Ifi204
Apoe	Transporter	Inhibited	-4.048	11.14	**Hspa1b**, **Hmox1**, **Hspa1a**, Serpina3n, Cxcl2, **Ddit3**, Ccl2, Il1rn, Ccn2, **Atf3**
Irf2bp2	Transcription Regulator	Inhibited	-4.094	9.55	**Hmox1**, Hcn1, Serpina3n, Ccl9, Scimp, Fcgr4, Cd14, Mybl1, Mmp3, Pilra
Ttc39aos1	Other	Inhibited	-4.319	17.16	Ccl7, Ccl2, Oas3, Oas2, Ccl4, Ly6a, Apol9a, Ube2l6, Irf7, Ifitm3
Trex1	Enzyme	Inhibited	-4.349	16.36	**Cdkn1a**, Ifi27l2a, Panx1, Oas1g, Oas3, Oas2, Ly6a, S100a6, Ube2l6, Gpx1
Cited2	Transcription Regulator	Inhibited	-4.61	9.78	Ifrd1, Cxcl2, Ccl2, Il1rn, Pou3f1, Oas1g, Oas3, Scimp, Gadd45b, Fcgr4

Table 1: Cytosolic DNA sensing signaling proteins were predicted as upstream regulators of eDEGs. Top 25 upstream regulators, identified by Ingenuity Pathway Analysis (IPA), predicted to be activated or inhibited based on 11-dpi eDEG expression differences between *Lmna*-cKO and *Lmna*-cWT samples. Top 10 most differentially expressed eDEGs targeted by predicted upstream regulators are displayed. Bolded gene names indicate target molecules also identified in the protein-protein interaction network of subcluster CM3 DEGs overlapping eDEGs (shown in Figure 4G).